Syn-eruptive degassing of a single submarine lava flow: constraints on MORB CO_2 variability, vesiculation, and eruption dynamics

By

Dorene Samantha Nakata

B.A., Carleton College, 2008

Submitted in partial fulfillment of the requirement for the degree of

Master of Science
at the
MASSACHUSETTS INSTITUTE OF TECHNOLOGY
and the
WOODS HOLE OCEANOGRAPHIC INSTITUTION

June 2010

Signature of Author

Joint Program in Marine Geology and Geophysics
Massachusetts Institute of Technology
and Woods Hole Oceanographic Institution
May 21, 2010

Certified by

S. Adam Soule
Thesis Supervisor

Accepted by

Bradford Hager
Chair, Joint Committee for Marine Geology and Geophysics
Massachusetts Institute of Technology
and Woods Hole Oceanographic Institution

Syn-eruptive degassing of a single submarine lava flow: constraints on MORB CO_2 variability, vesiculation, and eruption dynamics

By

Dorene Samantha Nakata

Submitted to the Department of Marine Geology and Geophysics on
May 21, 2010 in Partial Fulfillment of the Requirements for the
Degree of Master of Science in Marine Geology and Geophysics

ABSTRACT

Mid-ocean ridge basalts (MORBs) exhibit a wide range of CO_2 concentrations, reflecting saturation to supersaturation (and rarely undersaturation) relative to their emplacement depths. In this study, we explore the mechanisms of CO_2 degassing and the implications this has for estimating the advance rates and durations of seafloor eruptions. We present dissolved volatile concentrations (mainly of CO_2 and H_2O) and vesicle size distributions (VSDs) for a unique suite of MORB glasses collected at the East Pacific Rise, ~9° 50′ N. These MORB glasses were collected at ~200 m intervals along an across-axis track over a single flow pathway within the recently emplaced 2005-06 eruption boundaries; systematic sample collection provides one of the first opportunities to characterize intra-flow geochemical and physical evolution during a single eruption at a fast-spreading ridge. Compared to measurements of MORB volatiles globally, dissolved H_2O concentrations are relatively uniform (0.10 - 0.16 weight percent), whereas dissolved CO_2 contents exhibit a range of concentrations (154 - 278 ppm) and decrease with distance from the EPR axis (i.e., eruptive vent). Ion microprobe analyses of dissolved volatiles within the MORB glasses suggest that the magma erupted supersaturated (pressure equilibrium with 920 - 1224 mbsf) and in near-equilibrium with the melt lens of the axial magma chamber (~1250 - 1500 mbsf), and degassed to near equilibrium (299 - 447 mbsf) with seafloor depths over the length of the flow. The decrease in CO_2 concentrations spans nearly the full range of dissolved CO_2 contents observed at the EPR and shows that the varying degrees of volatile saturation that have been observed in other MORB sample suites may be explained by degassing during emplacement. Vesicularity (0.1 - 1.2%) increases with decreasing dissolved CO_2 concentrations. We use vesicle size distributions (VSDs)—vesicle sizes and number densities—to quantify the physical evolution of the CO_2 degassing process. VSDs suggest that diffusion of CO_2 into preexisting vesicles, and not nucleation of new vesicles, is the dominant mechanism of increasing CO_2 in the vapor phase. We also use VSDs, along with estimates of vesicle growth rates, to constrain emplacement time of the 2005-06 eruption to <~24 hours and to resolve variations in advance rate with downflow distance.

Thesis Supervisors: S. Adam Soule, Alison Shaw, Frederick Frey
Titles: Associate Scientist (WHOI), Associate Scientist (WHOI), Professor (MIT)

1. INTRODUCTION

Variations in mid-ocean ridge basalt (MORB) volatile concentrations trace the degassing of magmas from crustal reservoirs to seafloor. During equilibrium degassing, dissolved volatile concentrations follow Henry's Law and, in addition to melt composition, are strongly dependent on pressure and the relative concentrations of dissolved H_2O and CO_2 [*Dixon*, 1995; *Dixon et al.*, 1988; *Dixon et al.*, 1995]. As overlying pressure decreases during ascent, volatile solubility decreases in the melt, resulting in the exsolution of volatiles into vesicles. Contrary to Henrian behavior, MORBs exhibit a range of volatile concentrations, indicating disequilibrium with ambient seafloor pressures (i.e. eruption depths) and commonly exhibit supersaturation of CO_2 (Figure 1) [*Cushman et al.*, 2004; *Dixon et al.*, 1988; *Fine and Stolper*, 1986; *Le Roux et al.*, 2006; *Simons et al.*, 2002; *Standish et al.*, 2008]. Detailed studies at the fast-spreading East Pacific Rise (EPR) indicate that lava samples are often supersaturated near the axis, but have concentrations closer to their equilibrium saturation levels off-axis [*Le Roux et al.*, 2006]. There are two end-member models proposed to explain this variability: (1) in *decompression-controlled degassing*, the extent of degassing is dependent on ascent velocity and the length of the ascent pathway; (2) during *syn-emplacement degassing*, magma that is supersaturated at the vent degasses at isobaric conditions toward equilibrium during flow along the seafloor. Both of these models suggest that the kinetics of degassing lag behind the dynamic change in pressure during a MOR eruption, but differ in where the degassing occurs (i.e., conduit or seafloor). It is

possible that both models may apply to any single seafloor eruption, however neither has been verified by experiment or observation.

In this study, we examine a suite of lava samples collected along a single flow pathway within a recent eruption at the axis of the EPR at ~9° 50′ N to evaluate the range in volatile concentration and how that concentration varies during emplacement. Sampling along the lava flow pathway provides a unique opportunity to examine a suite of samples derived from a single magmatic source that have CO_2 supersaturation as an initial condition, but have spent varying amounts of time at seafloor pressures under nearly isothermal conditions.

As a MOR segment that has been extensively studied and has had at least two recently documented eruptions in 1991-92 and 2005-06 [*Gregg et al.*, 1996; *Haymon et al.*, 1993; *Soule et al.*, 2007; *Tolstoy et al.*, 2006], the EPR at 9°50′ N provides an optimal setting to investigate degassing processes during an eruption. The most recently documented volcanic event at the EPR occurred in late 2005, early 2006 [*Tolstoy et al.*, 2006]. Several coordinated research cruises beginning in April 2006 were able to collect data within a year of the eruption: workers used seafloor photos, *Alvin* dive video, sidescan sonar images, and lava samples to map the extent and internal morphological features of these new flows [*Fundis et al.*, in review; *Soule et al.*, 2007] and evaluate the geochemical variability within this eruption relative to the longer term variability at the ridge crest [e.g., *Goss et al.*, 2010]. Approximately twenty-one samples were collected along a single flow pathway within the 2005-06 eruption boundaries by *Jason II*, Dive 268 (*JII*-268).

Until this 2005-06 eruption, degassing mechanisms and vesiculation dynamics in MOR eruptions have been difficult to evaluate, as there were no natural datasets to verify models. The sampling method of the *JII*-268 suite allows us to systematically track the geochemical and physical evolution of erupted lava, and the relationship between both, over the ~2.5 km length of the flow. In addition to identifying the range of volatile concentrations preserved in a single eruption, we use quantitative analysis of vesicles – vesicle size distributions (VSDs) – to determine the time scale and mechanisms of volatile exsolution.

We find that the volatile concentrations in samples at or near the eruptive vent reflect supersaturation relative to seafloor depths (2503 - 2558 mbsf) and saturation equilibrium with depths of 920 - 1224 mbsf, corresponding to the approximate depth of the axial melt lens beneath the ridge crest (~1250 - 1500 mbsf) [*Detrick et al.*, 1987; *Detrick et al.*, 1993; *Harding et al.*, 1993; *Kent et al.*, 1993]. Samples near the flow boundary, ~2500 m from the vent, are nearly at equilibrium with seafloor pressures, showing saturation depths equivalent to 299 - 447 mbsf. Our results demonstrate that some portion of the overall variability in dissolved volatile concentration in MORB is achieved by equilibrium degassing at the seafloor after lavas have been erupted, and we propose that this degassing may be used as a geo-speedometer of volcanic processes. Our analysis of the vesicle size distribution and previous estimates of vesicle growth rates in MORB allow us to infer the relative rates of lava flow advance across the seafloor as a function of distance from the vent; we loosely constrain the duration of flow emplacement to ~24 hrs. We also conclude that vesicle growth occurs primarily through

exsolution of volatiles into existing vesicles. In addition, this data set represents one of the few examples of degassing of otherwise geochemically homogeneous lava, and as such has important implications for the behavior of other volatile species that are commonly believed to track CO_2 exsolution and/or vesicularity in basaltic magmas (e.g., He, Ar, Ne) [*Paonita and Martelli*, 2007].

2. 2005-06 ERUPTION

The 2005-06 eruption occurred between 9° 46 - 56′ N along the axis of the EPR, overprinting flows from the previously documented 1991-92 eruption. Seismic monitoring of the area between 2003 and 2006 revealed a buildup of microseismicity, culminating in an eruptive event during late 2005-early 2006 [*Tolstoy et al., 2006*]. In a multi-disciplinary effort to observe and characterize this seafloor eruption, a series of research cruises were deployed to the area beginning in April 2006. The twenty-one samples used in this study are a subset of twenty-five samples collected by *Jason II* (Dive 268) during an *R/V Atlantis* cruise (AT15-17) in April 2007.

Using TowCam imaging surveys [*Fornari*, 2003] and pre- and post-eruption sidescan sonar images of the 9° 50′ N region, *Soule, et al.* [2007] mapped the spatial extent of the 2005-06 lava flows. Mapping shows that the eruption extends ~18 km along the EPR axis, covering an area of ~14.6 km^2. The *JII*-268 samples were collected from an across-axis track along the farthest-reaching single flowpath, between 9° 50.5 - 51.5′ N (Figure 2, Table 1). This area, referred to as the "9° 51′ N flow lobe" in *Fundis, et al.* [in review], is characterized by an abundance of hackly and sheet flows (~70 % of the flow lobe) at and near the axis, which transition to lobate flows and eventually pillow

mounds at the flow boundary. This morphology is indicative of relatively rapid lava effusion and flow advance rates.

To reinforce visual observations that the *JII*-268 samples represent a single flow path, geochemical analyses were performed to evaluate the samples' compositional variability. The samples were analyzed for major elements on an electron microprobe at the USGS in Denver [for detailed methods, see *Goss et al.*, 2010] and for trace elements on an Element2 ICP-MS at the University of Florida. Major element analysis shows that there is relatively little variation in Fe-Mg content of the samples relative to the variability observed within the 2005-06 flow [*Goss et al.*, 2010], and relative to the larger scale variability of the EPR, 9 - 10° N [*Perfit*, unpublished data] (Figure 3). Geochemical homogeneity of the samples with respect to major element concentrations—particularly the lack of variability in Mg-content—indicates that differentiation of the melt did not occur over the length of the flow. Olivine or plagioclase crystallization would result in a systematic trend of increasing FeO content with decreasing MgO content.

Trace element concentrations exhibit a lack of variation that agrees with the geochemical homogeneity indicated by major element analysis. Trace element concentrations in the *JII*-268 MORB glasses exhibit depletion of light REEs and flat middle to heavy REEs relative to the primitive mantle, patterns typical of N-MORB (Figure 4). We do not observe statistically significant changes in MgO, Ni, and trace elements with distance from the axis (Figure 5), indicating no crystallization took place during transport and that lava emplacement was isothermal. Sample *JII*-268-01 (~843 m

west of the axis) is an exception to this analysis, and has trace element concentrations that are statistically lower than the rest of the 9° 51′ N flow lobe samples; this sample may represent the product of another flow path, as it was collected at the termini of the flow where eruption boundaries may be difficult to identify. Uniform trace and major element concentrations throughout the flow lobe suggest that the samples originate from a single pulse/batch of magma. Mapping and geochemical homogeneity of the *JII*-268 samples indicate that they are products of a single lava flow within the 2005-06 series of eruptions.

3. METHODS

3.1 Sample Collection

The twenty-one MORB samples were collected on an across-axis track of the 9° 51′ N flow lobe, along the widest single-flow path of the 2005-06 eruption. Samples were collected at ~200 m intervals, ~1 km west and ~2.5 km east of the axial summit trough (i.e., eruptive vent) (Figure 2). The sample locations were chosen based on the location of lava channels imaged by sonar backscatter that mark the primary flow pathways. This collection method allows us to document systematic changes in the flow as it progressed away from the axis.

The upper surfaces of the MORB samples are characterized by 2 - 22-mm thick glassy crusts formed by quenching of the lava during contact with seawater. The volatile and vesicle properties of the quenched glass best record the chemical and physical properties of the lava at the instant the flow reached a given distance from the vent. Based on our understanding of submarine lava flow emplacement, we expect that the

samples collected near the vent represent the first erupted material and the samples at the distal end represent the last erupted material. Regardless of timing, it is certain that the distal material experienced a longer time period in a molten state at seafloor pressures.

3.2 Volatile Analyses

For each of the MORB samples, we collected glass from the uppermost surface of the quenched layer. Glass fragments were polished and mounted in Indium metal for ion microprobe analysis. Analyses of dissolved volatile concentrations (CO_2, H_2O, F, S, Cl) in the MORB glasses were carried out on a Cameca IMS 1280 ion microprobe at the Northeast National Ion Microprobe Facility. The ion microprobe was calibrated with a number of standards including: ALV 519-4-1, 51-3, 46D, 1649-3, D20-3, JD17-H, 1654, 6001, and D52-5. Following the methods outlined in *Hauri, et al.* [2002] and *Shaw, et al.* [2010], absolute volatile concentrations were determined by comparing the ratio of the volatile in question to Si content, and subsequently comparing this ratio to standard calibration curves. Based on repeated use of the instrument at the facility, sample error is estimated to be ~10%. One to three measurements were made on each of the MORB glass chips, and in some cases on multiple chips from the same sample.

In addition to dissolved volatile concentrations, we also measured helium abundances and isotope ratios in the MORB glasses and vesicles, as helium and CO_2 are thought to partition from the melt similarly during the degassing process [*Marty and Jambon*, 1987]. ^{3}He and ^{4}He in the vapor (i.e., vesicles) and melt were determined by crushing and melting 15 of the *JII*-268 samples (following the methodology of *Kurz, et*

al. [2004] using blank measurements of 2 - 5 x 10^{-11} cm^3 STP ^4He), which were collected east of the vent.

3.3 Vesicle Population

Changes in the dissolved volatile content of the lava should be reflected in changes in the vesicularity of the MORB glasses. We use the VSD to quantify parameters such as total vesicularity, characteristic vesicle size, and vesicle number density to assess how the vesicle population changes with distance (i.e. time) and changing volatile concentration. The VSD of the *JII*-268 suite is used to determine whether exsolved volatiles are retained by the lava in vesicles, the mode of degassing (i.e., accommodating the increase in vapor phase by vesicle growth or nucleation), and to estimate lava advance rate and eruption duration.

A standard petrographic thin section of the quenched glassy crust was made for each sample. For each section, we took approximately seven non-overlapping photographs of the glassy crust at 2.5x magnification (e.g., Figure 6). We used image-analysis software (ImageJ, rsbweb.nih.gov/ij/) to identify and count the number of vesicles and the area of each vesicle within each image. ImageJ calculates the area of each identified vesicle, and the vesicle diameter is simply taken to be $2\sqrt{A/\pi}$. Ideally this 2-D analysis would closely reflect the 3-D VSD, however this relationship is distorted by two factors during the sampling process: (1) a thin section plane will not necessarily intersect a vesicle along a great circle, resulting in a measured vesicle diameter that is smaller than the actual vesicle size, and (2) relatively smaller vesicles are less likely to be sampled by a thin section plane compared to larger vesicles; as a result a 2-D VSD will

indicate a lower number of small vesicles and a higher number of large vesicles relative to the actual 3-D population. To resolve the actual size of each vesicle, we multiply the measured diameter by 1.176. This scaling factor is the result of studies by *Cashman and Marsh* [1988], which showed that the average measured diameter represents 0.85 of the actual vesicle diameter. To compensate for the sampling bias we follow the methods of *Cheng and Lemlich* [1983] and *Cashman and Mangan* [1994], and divide the vesicle population of each image into size (vesicle diameter) classes; subsequently, the number density (N_A) of each size class is divided by the average diameter of that size class, giving the number of vesicles per unit volume (N_V). This increases the number of small vesicles relative to large vesicles in a given volume of melt.

Using a population density function, we can model the 3-D VSD to understand the kinetics of vesicle formation during flow. The following population density function was originally employed by *Marsh* [1988] to model crystal growth dynamics, and later employed by *Mangan et al.* [1993] and *Cashman and Mangan* [1994] to model vesiculation:

$$n = n^{\circ}\exp(-L/G\tau) \tag{1}$$

where n, the volumetric number density, is

$$n = N_V/\Delta L \tag{2}$$

n° is the volumetric number density of nuclei, L is the vesicle diameter, G is the average vesicle growth rate, and τ is the time needed for vesicle growth and volatile degassing. The relationship between ln n and L will be linear and will have a y-intercept of n° and a slope of $-1/G\tau$.

4. RESULTS

4.1 Volatile Measurements

In this study, we make a distinction between dissolved volatiles (in the melt) and exsolved volatiles (vapor in vesicles). Dissolved volatile concentrations (CO_2, H_2O, F, S, Cl) of MORB glasses from the 2005-06 eruption are shown in Table 2. With the exception of CO_2, dissolved volatile concentrations show no statistically significant variation within the suite of samples or systematic variations along the flow pathway: H_2O 0.10 - 0.16 (±0.01) wt. %; S 1023 - 1153 (±100) ppm; F 95 - 127 (±10) ppm; Cl 61 - 81 (±7) ppm (outlier *JII*-268-19 shows a measured dissolved Cl concentration of 9.5 ppm).

The MORB glasses exhibit a significant variation and a systematic decrease in dissolved CO_2 content from 236 - 278 ppm near the axis to 154 - 174 ppm up to ~2.5 km away. Dissolved CO_2 does not decrease gradually over the flow: CO_2 is relatively uniform for the first ~800 - 1170 m; beyond this near-axis region, CO_2 decreases sharply over a distance of 100 - 450 m; beyond 1250 m distance from the axis, CO_2 concentrations are relatively uniform but significantly lower than near-axis concentrations.

Dixon, et al., [1995] performed a series of isothermal experiments (1200 °C) to determine the pressure and composition dependent CO_2 and H_2O solubilities in basaltic melts. Using these experimental findings, *Dixon* [1995] devised a model to determine the equilibrium saturation pressure of a melt (i.e. pressure of vapor-melt equilibrium) based

on measured CO_2 and H_2O in basaltic glasses. The solubility and exsolution of C-species between the vapor and melt is described by the following reaction:

$$CO_2(vapor) + O^{2-}(melt) \Leftrightarrow CO_3^{2-}(melt)$$

Assuming CO_2 and H_2O are the only species in the vapor phase then:

$$\frac{X^m_{H_2O,mol}}{X^{o,m}_{H_2O,mol}} + \frac{X^m_{CO_3^{2-}}}{X^{o,m}_{CO_3^{2-}}} = 1 \tag{3}$$

where

$$X^m_{H_2O,mol} = X^m_{H_2O,mol}(P_0,T_0)\frac{f_{H_2O}(P,T_0)}{f_{H_2O}(P_0,T_0)}\exp\left[\frac{(-V^{o,m}_{H_2O})(P-P_0)}{RT_0}\right] \tag{4}$$

$$X^{o,m}_{H_2O,mol} = X^{o,m}_{H_2O,mol}(P_0,T_0)\frac{f^o_{H_2O}(P,T_0)}{f^o_{H_2O}(P_0,T_0)}\exp\left[\frac{(-V^{o,m}_{H_2O})(P-P_0)}{RT_0}\right] \tag{5}$$

$$X^m_{CO_3^{2-},mol} = X^{o,m}_{CO_3^{2-},mol}(P_0,T_0)\frac{f_{CO_2}(P,T_0)}{f_{CO_2}(P_0,T_0)}\exp\left[\frac{(-V^{o,m}_r)(P-P_0)}{RT_0}\right] \tag{6}$$

$$X^{o,m}_{CO_3^{2-},mol} = X^{o,m}_{CO_3^{2-},mol}(P_0,T_0)\frac{f^o_{CO_2}(P,T_0)}{f^o_{CO_2}(P_0,T_0)}\exp\left[\frac{(-V^{o,m}_r)(P-P_0)}{RT_0}\right] \tag{7}$$

[*Dixon*, 1995; *Dixon et al.*, 1997; *Dixon et al.*, 1995]. See Table 3 for definitions of parameters and values used.

We determined equilibrium saturation pressures of the MORB glasses from the measured concentrations of dissolved CO_2 and H_2O (Figure 7) using the program VolatileCalc [*Newman and Lowenstern*, 2002], which is based on the model described above. Calculations show that CO_2-H_2O concentrations correspond to equilibrium saturation pressures of 512 - 599 bars at the axis to 336 - 378 bars at the distal end of the

flow, ~1250-2500 m away (Figure 8). Based on the following equation, we determine the corresponding equilibrium saturation depth for each calculated pressure:

$$P_{total}(\frac{kg}{m\cdot s^2}) = \rho_{water} g z_{water} + \rho_{crust} g z_{crust} + 101{,}325 \frac{kg}{m\cdot s^2} \quad (8)$$

P_{total} is the total equilibrium saturation pressure calculated using the model described above, water density (ρ_{water}) is 1000 kg/m^3, crustal density (ρ_{crust}) is 2900 kg/m^3, g is 9.8 m/s^2, and z is the depth of each medium, which for water is 2503 - 2558 m. The modeled saturation pressures indicate that samples near the axis are at equilibrium with depths of 920 - 1224 mbsf, and samples at the end of the flow have are at equilibrium with depths of 299 - 447 mbsf. Saturation pressures and depths are listed in Table 4.

4.2 2-D Vesicle Data

Two-dimensional vesicle measurements for samples from the 2005-06 eruption are shown in Table 5. Measured vesicularity increases from 0.08 to 1.17 % over the length of the flow (Figure 9). These low vesicularity measurements are typical for the 2005-06 flow [*Soule et al.*, 2007]. As previously discussed, individual vesicle sizes are scaled by a factor of 1.176 to account for the discrepancy between actual and measured vesicle diameter. Based on this correction factor, vesicle sizes range from 0.0032 - 0.21 mm. Size-frequency histograms indicate that vesicle sizes are skewed toward smaller size fractions. These histograms show that 50% of vesicles are equal to or smaller than one-third of the largest measured vesicle in each of the thin section images. Measured vesicle densities range from 5 to 52 vesicles/mm^2, with no statistically significant variation.

4.3 Corrected Vesicle Data

In addition to correcting for discrepancies between the apparent and actual vesicle size, we must also account for the sampling bias wherein smaller vesicles are less likely to be intersected by a thin section plane than larger vesicles and are therefore underrepresented by thin section image analysis. To account for this bias, the number of vesicles in each size class is divided by the average diameter of that size class; this increases the number of smaller vesicles relative to the number of larger vesicles. The results of applying these series of corrections are represented as a plot of ln n vs. L (e.g. Figure 10) for each thin section image, where n is the number of vesicles per volume per size class (mm^{-4}) and L is the diameter (mm). By crystal size distribution theory, the slope of a linear fit to ln n vs. L is equivalent to $-1/G\tau$, where G is the growth rate (mm/s) and τ is the duration of vesicle growth (s). Variations of this plot were created for each of the 138 thin section images using 12, 15, and 18 equivalent size classes. Multiple bin schemes were used to eliminate any bias from using only one bin size, as the derivation of n and n^o involves an exponential function which may be sensitive to small changes in ln n. The qualitative shape of each plot is a negatively sloping line; in the majority of profiles there is a perturbation in this line, such that the plot of ln n vs. L is described by two adjoining negatively sloping segments. For each plot, the slope $-1/G\tau$ is calculated using the line segment from 0.0 mm, which represents a much larger fraction of the total number of vesicles. The number of size classes used to determine the extent of this line segment (i.e., the largest vesicles included in the linear fits) is the maximum number of data points required to ensure that a linear regression from 0.0 mm has an R^2 of at least

0.8. Calculated values for $G\tau$ are 4.93 - 13.1 x 10^{-3} mm, 2.88 - 13.2 x 10^{-3} mm, and 1.74 - 16.1 x 10^{-3} mm for 12, 15, and 18 bins, respectively. Values of n^o are 7.52 - 134 x 10^4 mm^{-4}, 7.46 - 134 x 10^4 mm^{-4}, and 7.31 - 975 x 10^4 mm^{-4} for 12, 15, and 18 bins respectively. A weighted average and standard deviation value of $G\tau$ and n^o for each sample are subsequently calculated from the three bin schemes (Table 6).

4.4 Helium Variability with Respect to CO_2 and Vesicularity

As a preliminary attempt to understand the degassing of CO_2 relative to noble gases, we have performed crushing and melting experiments to measure helium concentration and isotope ratios for the 15 samples located east of the vent (Table 7). Total helium content is 2.07 ± 1.24 x 10^{-5} cm^3 STP/g and $^3He/^4He_{melt}$ is 8.47 ± 0.10; these values are consistent with previous measurements of EPR glasses from the 1991-92 eruption [*Gregg et al.*, 2000]. The *JII*-268 sample collection method allows us to characterize variations in helium, in both vesicles and melt, with respect to the evolution of CO_2 loss and vesiculation in a single batch of magma for the first time. The fraction of total ^4He in vesicles ranges from 0.07 to 0.51, increasing over the length of the lava flow, and co-varies with vesicularity (Figure 11). Furthermore, ^3He decreases in the melt, co-varying with dissolved CO_2. This indicates that exsolution of helium is suppressed while the melt is still supersaturated with respect to CO_2 near the axis; He partitions into the vapor phase during CO_2 exsolution (as He cannot partition out of the melt on its own). Partitioning of helium likely reflects variations in vesicle content as much as dissolved CO_2 content [*Kurz and Jenkins*, 1981].

We measure $C/^3He$ in the 2005-06 MORB glass to be $6.99 \pm 0.54 \times 10^8$. While this value is an order of magnitude lower than that determined by *Marty & Jambon* [1987] at 2×10^9, recent studies have noted a link between $C/^3He$ ratio and MORB chemistry. Based on measurements of MORB glasses from the EPR and Mid-Atlantic Ridge, *Marty & Tolstikhin* [1998] observed higher $C/^3He$ ratios in E-MORB ($3.3 \pm 1.1 \times 10^9$) compared to N-MORB ($8.6 \pm 2.4 \times 10^8$). This higher $C/^3He$ in E-MORB possibly reflects an upper mantle source with a recycled component (from subduction) that results in the enrichment of light REEs as well as CO_2. Normalized REE patterns (relative to chondritic values in *Sun & McDonough* [1989]) for the 2005-06 flow are consistent with relative N-MORB concentrations [*Goss et al.*, 2010], and our calculated values of $C/^3He$ for the 9° 51′ N flow lobe are consistent with other N-MORB samples measured by *Marty & Tolstikhin* [1998]. Determination of variations in the $C/^3He$ ratio is significant as it provides potential insight into variations in carbon concentration in mantle sources. The low $C/^3He$ ratio in the 2005-06 samples relative to the canonical value and the ratio determined by E-MORB likely indicates a mantle composition with low CO_2 content compared to global MORB sources.

5. DISCUSSION

5.1. Single Flow Pathway of the 2005-06 Eruption

Homogeneity of major (Figure 3) and trace element analyses (Figure 4) [*Goss et al.*, 2010] in addition to mapping of the flow [*Soule et al.*, 2007], provides strong indication that the *JII*-268 samples are products of a single eruption of a single magma source. The lack of any statistically significant variations in MgO, Ni, and incompatible element concentrations in the melt (Figure 5) precludes the likelihood of fractional crystallization during emplacement, and suggests isothermal conditions for the flow. Additionally, flow morphology near the axis is dominated by sheet and hackly flows [*Fundis et al.*, in review]: sheet flows have a smooth, ropy texture and are the typical morphology of lava channels; hackly flows, also known as "jumbled sheet flows" have a texture analogous to 'a'a flows in subaerial settings. Both flow morphologies indicate rapid flow advance rates and likely high effusion rates at the vent. While variations in CO_2 content near the vent (<~1000 m distance from the axis) likely result from minor fluctuations in ascent rate, an overall rapid ascent rate indicated by the sheet-dominated flow morphology suggests that the large-scale variability of dissolved CO_2 over the length of the flow is not likely a result of a highly variable magma ascent rate throughout the eruption.

5.2 CO_2 Degassing

The solubilities of CO_2 and H_2O in melts are composition and pressure dependent. Given the homogeneity of MORB samples from this portion of the EPR [*Smith et al.*, 2001], volatile systematics provide meaningful tools for tracking the degassing of basaltic

melts during transport from storage in crustal reservoirs to emplacement at the seafloor. If consistent with Henrian behavior, the solubilities of these volatiles should decrease with decreasing lithostatic or magmastatic pressure during ascent; in this case of "equilibrium degassing," a melt is always in saturation equilibrium with its current depth. Assuming CO_2 and H_2O are the main constituents of the vapor phase [*Dixon*, 1995; *Dixon et al.*, 1995; *Fine and Stolper*, 1986] their concentrations in MORB glass should reflect this pressure of equilibrium saturation. As all samples from the 2005-06 eruption are collected at the seafloor at 2503 - 2558 mbsl (246 – 252 bars), dissolved CO_2 and H_2O concentrations should be consistent with this depth range.

At melt-vapor equilibrium, magma at a given depth can have a range of CO_2:H_2O concentration ratios [see Figure 1 in *Dixon*, 1995]. For samples at a single depth, higher concentrations of dissolved H_2O result in relatively lower solubility and thus concentrations of CO_2. From ion microprobe analyses, we observe that water concentrations (0.13 ± 0.01 weight percent) do not vary significantly or systematically over the distance of the flow (Table 2). This is expected, as H_2O is highly soluble and therefore undersaturated in MORB melts; significant changes in dissolved H_2O content are unlikely at water depths greater than 500 mbsl [*Moore*, 1965; *Moore et al.*, 1977]. With measured H_2O contents of 0.10 - 0.16 weight percent and at the known eruption pressure range, the *J11*-268 samples should have similarly homogeneous dissolved CO_2 concentrations of ~110-120 ppm, lower than the measured values for this dataset. However, a number of studies observe that a majority of MORB samples have CO_2 concentrations that indicate incomplete degassing (i.e., supersaturation relative to their

eruption depths) [*Cushman et al.*, 2004; *Dixon et al.*, 1988; *Le Roux et al.*, 2006; *Simons et al.*, 2002; *Standish et al.*, 2008]. Only under unique circumstances do MORB samples exhibit undersaturation of CO_2 (e.g., study of melt inclusions by *Saal, et al.* [2002]). A number of factors have been proposed to explain these variable extents of degassing, including: (1) residence time in a magma chamber [*Sarda and Graham*, 1990]; (2) length of the ascent pathway to the surface and ascent rate [*Dixon*, 1995; *Dixon et al.*, 1988]; and (3) flow rate and length of the flow pathway, either on the seafloor surface or in lateral sub-surface conduits [*Dixon et al.*, 1988]. In the case of supersaturation, it is assumed that the kinetics of degassing are slow relative to the rate of depressurization of the magma from its last depth of saturation equilibrium. Samples in saturation equilibrium with their emplacement depths can be explained by relatively slow ascent rate and/or degassing of magma along the seafloor surface.

CO_2 and H_2O concentrations for samples at or near the vent (within ~802 - 1170 m) indicate equilibrium saturation pressures of 512 - 599 bars (920 - 1224 mbsf). These pressures are similar to that of the axial magma chamber at ~601 - 672 bars (~1250 - 1500 mbsf [*Detrick et al.*, 1987; *Detrick et al.*, 1993; *Harding et al.*, 1993; *Kent et al.*, 1993; *Sinton and Detrick*, 1992; *Toomey et al.*, 1990]). Off-axis samples (>1250 m from the vent) have volatile concentrations in saturation equilibrium with pressures of 336 - 378 bars (consistent with 299 - 447 mbsf), similar to the range of ambient seafloor pressures. The results of this natural dataset suggest that magma from the 2005-06 eruption reached saturation equilibrium in the magma chamber, experienced minimal degassing during ascent to the seafloor, erupted supersaturated with respect to CO_2, and

degassed towards equilibrium with ambient seafloor pressures during flow along the seafloor.

During this syn-eruptive degassing process, CO_2 is not exsolved at a constant rate (i.e., CO_2 concentrations do not smoothly decrease along the length of the flow). Instead, the lava stays supersaturated for ~802 - 1170 m from the vent, and then CO_2 concentrations decrease exponentially over the next ~1250 - 1700, with a large portion of the degassing occurring over ~100 - 450 m. CO_2 concentrations never quite reach equilibrium with seafloor pressures but appear to degas slowly towards the distal end of the flow (Figure 8). Supersaturation near the axis suggests that the lava flow rate is at least as high as the ascent rate, as degassing was suppressed during transport up to the seafloor, and samples remain supersaturated near the axis. A relatively high ascent and flow rate for this area is supported by the sheet and hackly morphology observed by *Fundis, et al. [in review]*. At ~802 - 1170 m from the vent, degassing of CO_2 initiates suggesting that flow advance rate decreased to a slow enough rate to allow CO_2 exsolution or that enough time had passed to allow degassing to be resolved in the dissolved CO_2. In the distal portion of the flow, we attribute the slight supersaturation of the samples to a low CO_2 chemical gradient between the melt and vapor phases: a lower degree of supersaturation after the initial degassing period slows CO_2 exsolution over the remaining length of the flow. Such behavior is observed in models of diffusion-controlled vesiculation [e.g. *Sparks*, 1978].

Sample *JII*-268-24 (~2418 m from axis) exhibit dissolved CO_2 concentrations higher than expected given the overall degassing trend (Figure 8). It was noted during

sample collection that this sample may not have come from the 2005-06 eruption due to a difference in sediment accumulation. This is supported by the difference in $C/^3He$ in this sample relative to the others (Table 7). Although we believe this sample to represent an older eruption, we include it for completeness.

One of the most significant findings of this study are that the dissolved CO_2 concentrations within the *JII*-268 MORB glass samples from a single eruption span the range of CO_2 concentrations (and supersaturations) observed in the much more aerially extensive EPR 9 - 10° N sample suite containing samples from dozens of eruptions [*Le Roux et al.*, 2006]. One can conclude that volatile concentrations from a single sample do not adequately reflect volatile concentrations of the entire deposit. Furthermore, we conclude that the CO_2 variability arises from degassing of a supersaturated lava during emplacement, and that this process is likely an important contributor to the overall variability in dissolved CO_2 in MORBs. Below we discuss the mechanisms and rates of CO_2 degassing during emplacement.

5.3 2-D Vesicularity

As CO_2 is the main constituent of the vapor phase [*Dixon*, 1995; *Moore et al.*, 1977], changes in the vesicle population of the 2005-06 eruption samples (i.e., number or size of vesicles) should reflect the observed loss of CO_2 from melt to vapor during the lava flow's advance across the ridge crest. 2-D vesicle measurements of the MORB glass images show that vesicularity (volume percent) increases from 0.1 to 1.2 % over the length of the flow; while typical of the EPR, these vesicularities are considered low in the range observed in submarine basalts [*Dixon et al.*, 1988; *Gregg et al.*, 2000; *Moore et al.*,

1977] which are <10%, and up to 18% in the case of Mid-Atlantic Ridge popping rocks [*Sarda and Graham*, 1990]. The ~1 % increase in vesicularity is of the magnitude predicted by CO_2 loss assuming ideal gas behavior:

$$PV = nRT \tag{9}$$

where P for each sample is the ambient seafloor pressure, n is the number of moles of CO_2 lost from the melt ($CO_{2\ sample} - CO_{2\ original}$), R is the gas constant, and T is constant at 1473.15 K (1200 °C) to reflect isothermal conditions. This result suggests closed-system behavior, in which dissolved CO_2 is lost to vesicles but neither vesicles nor total volatile content are lost from the flow altogether, and is supported by the strong correlation between vesicularity and CO_2 concentration (Figure 12). Evolution of the VSD in the 2005-06 eruption samples should therefore provide an accurate representation of the mode of vesicle growth as a result of volatile exsolution.

5.4 Mode of Vesiculation

To understand the evolution of the vesicle population in light of the observed CO_2 degassing, we have employed the crystal growth theory formulated by *Marsh* [1988], which was originally used to model changes in crystal size as a function of growth rate and age. A number of studies have since employed this model to vesicle data from subaerial and submarine environments to investigate degassing processes during ascent and eruption [*Blower et al.*, 2001; *Cashman et al.*, 1994; *Cashman and Marsh*, 1988; *Mangan et al.*, 1993; *Sarda and Graham*, 1990]. As with crystal growth theory, this method is used to model changes in vesicle size and density as a function of vesicle growth rate and time.

Linear fits to plots of ln n vs. L for measurements made from thin section images of the 2005-06 eruption MORB glass yield values of $G\tau$ (mm), an integrated average growth rate and timescale, and $n°$, the volumetric nuclei density (number of vesicles/ mm^4) for each sample. The dominant vesicle diameter (mm) is estimated as

$$L_D = G\tau \tag{10}$$

and the 3-D vesicle density (number of vesicles/ mm^3) is estimated as

$$N_T = n^o G\tau \tag{11}$$

[*Cashman and Mangan*, 1994; *Cashman et al.*, 1994; *Marsh*, 1988; *Randolph and Larson*, 1988]. The dominant vesicle diameter, L_D, for 2005-06 eruption samples range from 02.47 - 10.64 x 10^{-3} mm (Figure 13; Table 6). Dominant vesicle diameter shows a weak increasing trend during the eruption. The 3-D vesicle densities, N_T, for samples in the eruption suite are 0.78 - 8.26 x 10^3 vesicles/ mm^3, with no statistically significant trend to account for this variability (Figure 14; Table 6). It is worthwhile to note that because the vesicularity—and inherently the number and size of vesicles—is so low, the uncertainty of these measurements will be large relative to the overall variation within the flow. This presents some difficulty in discerning clear trends between vesicle size and number density with flow distance.

Changes in characteristic vesicle size and vesicle number density over the length of the flow provide insight into how vesicularity increases as a function of increasing vapor volume. As volatiles exsolve from the melt, the vesicle population must accommodate this increasing volume of vapor by *diffusion-controlled growth* and/or *nucleation* of new vesicles, each of which will have a unique manifestation on the vesicle

size distribution described above [*Proussevitch et al.*, 2007]. In the case of diffusion-controlled growth, volatiles exsolve into preexisting vesicles, and vesicle size—approximated by L_D—increases as a result. During nucleation, degassing is accommodated by the emergence of new vesicles, resulting in an increase in the vesicle number density, approximated by $n°G\tau$. In addition, an existing population of vesicles may be altered without the requirement of additional vapor by *coalescence* and/or *Ostwald ripening* [*Proussevitch et al.*, 2007]. During coalescence, two or more vesicles join to produce one larger vesicle. Ostwald ripening describes the process in which relatively larger vesicles grow at the expense of smaller vesicles by pressure-controlled diffusion. While coalescence and Ostwald ripening are not necessarily responses to degassing, their ability to alter the vesicle population make them significant processes to consider when analyzing the vesicle size distribution. Both processes are reflected as a decrease in number density of vesicles, and an increase in dominant vesicle diameter.

Analysis of the vesicle size distribution and MORB glass images suggests that diffusion is the dominant mechanism of vesicle growth during the eruption. The slight increase in 2-D vesicularity (Figure 9) and dominant vesicle size (Figure 13) indicate vesicle growth is occurring. The lack of any discernable increase in vesicle number density (Figure 14) precludes the likelihood of nucleation as a dominant process. If coalescence and Ostwald ripening were causing the increase in vesicle size, there would also be simultaneous decreases in vesicle number density, which we do not observe. Additionally, thin section images of the MORB glass samples do not exhibit any textures consistent with these processes. Furthermore, coalescence is a more dominant

mechanism in magmas with populations of larger bubbles [*Baker et al.*, 2006; *Cashman et al.*, 1994; *Gaonac'h et al.*, 1996].

5.5 Constraining Eruption Dynamics

The values of $G\tau$ provide an integrated measure of the average vesicle growth rate (G) and total time for vesicle growth (τ) of each sample. Using estimates of the vesicle growth rate, we attempt to determine the timescale of vesicle growth, which can subsequently be interpreted as the duration of the eruption. In their study of Mid-Atlantic Ridge popping rocks, *Sarda and Graham* [1990] estimated vesicle growth rates of 10^{-7} - 10^{-6} mm/s. First, we apply realistic estimates of lava flow rate to our measurements of $G\tau$ to evaluate this predicted range of vesicle growth rate. Having concluded that vesicle growth rate estimates are reasonable, we use models of vesicle growth to constrain eruption dynamics in the 2005-06 EPR eruption.

5.5.1 Evaluation of Vesicle Growth Rate Estimates

Estimated magma ascent rates for submarine eruptions range from 1×10^{-4} - 1×10^{-1} m/s [*Bottinga and Javoy*, 1991; *Gregg et al.*, 1996; *Mangan et al.*, 1993; *Sarda and Graham*, 1990]. While lava advance rate is linked to ascent rate, it can also be impacted by surface slope, focusing of the flow, and preexisting seafloor topography; we use the above ascent rates as proxies for advance rates as a simplification, understanding that there is some degree of limitation to these estimates. To evaluate the vesicle growth rate, we employ *constant* velocity models [e.g. *Mangan et al.*, 1993; *Sarda and Graham*, 1990] and *constantly decreasing* velocity models. Modeling a decreasing flow rate is meant to more appropriately depict a high flow rate at the vent, with the lava flow

slowing to a stop ~2500 m away due to decreases in eruption rate and/or a transition from focused flow at the vent to diffuse flow at the toe. For the two constant velocity profiles, we model flow advance rates of 1 x 10^{-4} and 1 x 10^{-1} m/s to capture the full range of assumed eruption rates, durations, and consequent vesicle growth rates. Using a constant velocity profile, the duration (τ) can be determined from the measured flow distance (*l)* and lava flow velocity (v) as $\tau = l/v$. An eruption with a flow advance rate of 1 x 10^{-4} m/s will take ~6700 hrs, and a flow advance rate of 1 x 10^{-1} m/s will require ~7 hrs. In addition, we also model the lava flow as having eruption rates of 1 x 10^{-4}, 1 x 10^{-3}, 1 x 10^{-2}, and 1 x 10^{-1} m/s at the axis, constantly decreasing in velocity to 0 m/s over a distance of 2418 m, the length of the flow. For a constantly decreasing lava flow velocity, the eruption duration (τ) is determined from the following equation:

$$x_{final} = x_{axis} + v_{axis}\tau + \frac{1}{2}\left(\frac{v_{final} - v_{axis}}{\tau}\right)\tau^2 \qquad (12)$$

where is x_{final} is 2418 m, x_{axis} is 0 m, v_{final} is 0 m/s, and v_{axis} is between 1 x 10^{-4} - 1 x 10^{-1} m/s. These constantly decreasing velocity profiles correspond to eruption durations of ~13000 hr, ~1300 hr, ~130 hr, and ~13 hr respectively. Eruption durations and resulting vesicle growth rate values are shown in Table 8; these models of vesicle growth are not meant to provide empirical growth rate values, but rather constrain the vesicle growth rate to orders of magnitude.

Resulting vesicle growth rates have orders of magnitude of 1 x 10^{-10} - 1 x 10^{-5} mm/s. With all models of velocity, vesicle growth rate (G) decreases during the eruption. This is expected, as vesicle growth rate should be greatest near the axis when the concentration gradient of CO_2 between the melt and vesicle population is greatest

[*Prousevitch et al.*, 1993] due to volatile supersaturation; as CO_2 reaches melt-vapor equilibrium and vesicles approach their final size, vesicle growth rate will decrease.

Based on comparisons to other predictions of MOR eruption emplacement times at the EPR [*Gregg et al.*, 1996; *Gregg et al.*, 2000], the models of constantly decreasing flow velocity from 1 x 10^{-2} and 10^{-1} m/s provide the most reasonable estimates of eruption duration, at ~130 and ~13 hr respectively. Based on these two models of eruption rate, the corresponding growth rates range between 10^{-5} - 10^{-7} mm/s. This encompasses the range of vesicle growth rates predicted by *Sarda and Graham* [1990] at 10^{-6} - 10^{-7} mm/s for Mid-Atlantic Ridge popping rocks.

5.5.2 Estimating the 2005-06 Eruption Duration

Values of $G\tau$ and estimates of magma flow rate suggest that vesicle growth rates by *Sarda and Graham* [1990] are reasonable for the 2005-06 eruption. Using their values to constrain vesicle growth rate models, we estimate the eruption duration and flow rates for the 2005-06 event. We model vesicle growth rate during the eruption in three modes: (1) a constant growth rate of 1 x 10^{-7} mm/s, (2) growth rate decreasing *linearly* from 1 x 10^{-6} to 1 x 10^{-7} mm/s, and (3) growth rate decreasing *exponentially* from 1 x 10^{-6} to 1 x 10^{-7} mm/s (Figure 15). The eruption duration is calculated as 3.7 hrs, 18 hrs, and 24 hrs, respectively, for the vesicle growth rate schemes described. Eruption velocity for each sample distance is determined from the equation $\tau = l/v$, where τ determined by applying one of the growth rate models above to the calculated values of $G\tau$, and l is the measured distance from the axis for each sample (Figure 16). For an eruption with a constant vesicle growth rate, flow velocity increases from ~0.01 m/s to ~0.35 m/s. A constant

vesicle growth rate is not expected from vesicle growth models due to decreases in supersaturation (i.e., chemical gradient) and changes in surface area to volume ratios with time. Accordingly, a constant bubble growth rate model produces an equally unlikely flow rate evolution (increasing flow rate with time/distance down flow) given that the flow ultimately stops. A decreasing vesicle growth rate, whether linearly or exponentially, results in an initial increase in eruption velocity from 0.01 m/s to ~0.06 - 0.1 m/s, followed by a decrease in flow velocity to ~0.03 m/s. Linearly and exponentially decreasing vesicle growth rate models provide the most reasonable estimates of eruption duration and lava flow velocity. Vesicle growth models [e.g., *Sparks*, 1978] suggest an exponentially decreasing vesicle growth rate. This model produces the most realistic down-flow velocity profile, similar to trends in eruption rate with time observed for basaltic volcanoes (e.g., Hawaii, Iceland, Etna [*Harris et al.*, 2000]) which show a marked peak in eruption rate early in the eruption followed by a rapid decay in eruption rate until the eruption ceases.

6. CONCLUSIONS

The *JII-268* MORB glass suite is the first dataset to provide the opportunity to understand the inherent geochemical and physical variability that develops within a single eruption along a single flow pathway. Based on geological observation and trace element geochemistry data, it is apparent that this flow pathway reflects the eruption and emplacement of a single parent magma. Based on our analysis of dissolved volatile concentrations and accompanying changes in lava vesicularity we conclude the following:

- The 2005-06 eruption was initially supersaturated with respect to CO_2, having equilibrium saturation pressures of 512 - 599 bars. The volatile content reached saturation in the magma chamber, at approximately 601 - 672 bars (1250-1500 mbsf), and degassed minimally during rapid ascent to the seafloor.
- The observed decrease in dissolved CO_2 concentrations indicates that the lava flow degassed toward saturation pressure in equilibrium with seafloor pressures during emplacement. Syn-emplacement degassing is the dominant process contributing to variability in CO_2 during the 2005-06 eruption from its initial supersaturated condition. This provides a possible explanation for the range of dissolved CO_2 concentrations observed in other MORB glasses from throughout the EPR 9 - 10 ˚N, and more specifically for the observed trends of decreasing volatile supersaturation with distance from the axis.
- Diffusion of CO_2 into an existing vesicle population is the dominant process controlling vesiculation of the melt during the eruption. The lack of strong, systematic trends in vesicle density, as well as textural evidence from sample thin-sections, preclude the likelihood that vesicle nucleation, coalescence, or Ostwald ripening contribute significantly to changes in the vesicle population.
- Based on models of vesicle growth rate, eruption velocities for this flow range from 0.01 - 0.1 m/s. This range in velocity, as well as the decreasing lava flow rate, correspond to estimated eruption times of <~24 hours.

ACKNOWLEDGEMENTS

I would like to thank Adam Soule and Mark Kurz for their insight on this project. I would also like to thank Nobu Shimizu, Andrey Gurenko, Alison Shaw, Nicole Keller, and Joshua Curtice for their help in collecting the volatile geochemistry data and Allison Fundis and Michael Perfit (U. Florida) for collection of major and trace element geochemistry data. Thanks to WHOI Academic Programs and the National Science Foundation (OCE-0732366 to S.A. Soule) for funding.

7. BIBLIOGRAPHY

Baker, D. R., P. Lang, G. Robert, J. F. Bergevin, E. Allard, and L. Bai (2006), Bubble growth in slightly supersaturated albite melt at constant pressure, *Geochemica et Cosmochimica Acta*, *70*, 1821-1838.

Blower, J. D., J. P. Keating, H. M. Mader, and J. C. Phillips (2001), Inferring volcanic degassing processes from vesicle size distributions, *Geophysical Research Letters*, *28*, 347-350.

Bottinga, Y., and M. Javoy (1991), The degassing of Hawaiian tholeiite, *Bulletin of Volcanology*, *53*, 73-85.

Cashman, K. V., and M. T. Mangan (1994), Physical aspects of magmatic degassing II, Constraints on vesiculation processes from textural studies of eruptive products, *Reviews in Mineralogy and Geochemistry*, *30*, 447-478.

Cashman, K. V., M. T. Mangan, and S. Newman (1994), Surface degassing and modifications to vesicle size distributions in active basalt flows, *Journal of Volcanology and Geothermal Research*, *61*, 45-68.

Cashman, K. V., and B. D. Marsh (1988), Crystal size distribution (CSD) in rocks and the kinetics and dynamics of crystallization II: Makaopuhi lava lake, *Contributions to Mineralogy and Petrology*, *99*, 292-305.

Cheng, H. C., and R. Lemlich (1983), Errors in the measurement of bubble size distribution, *Industrial and Engineering Chemistry Fundamentals*, *22*, 105-109.

Cushman, B., J. Sinton, G. Ito, and J. Eaby Dixon (2004), Glass compositions, plume-ridge interaction, and hydrous melting along the Galapagos Spreading Center, 90.5°W to 98°W, *Geochem. Geophys. Geosyst.*, *5*, Q08E17.

Detrick, R. S., P. Buhl, E. Vera, J. Mutter, J. Orcutt, J. Madsen, and T. Brocher (1987), Multi-channel seismic imaging of a crustal magma chamber along the East Pacific Rise, *Nature*, *326*, 35-41.

Detrick, R. S., A. J. Harding, G. M. Kent, J. A. Orcutt, J. C. Mutter, and P. Buhl (1993), Seismic Structure of the Southern East Pacific Rise, *Science*, *259*, 499-503.

Dixon, J. E. (1995), An Experimental Study of Water and Carbon Dioxide Solubilities in Mid-Ocean Ridge Basaltic Liquids. Part II: Applications to Degassing, *Journal of Petrology*, *36*, 1633-1646.

Dixon, J. E., D. A. Clague, P. Wallace, and R. Poreda (1997), Volatiles in Alkalic Basalts from the North Arch Volcanic Field, Hawaii: Extensive Degassing of Deep Submarine-erupted Alkalic Series Lavas, *Journal of Petrology*, *38*, 911-939.

Dixon, J. E., E. Stolper, and J. R. Delaney (1988), Infrared spectroscopic measurements of CO_2 and H_2O in Juan de Fuca Ridge basaltic glasses, *Earth and Planetary Science Letters*, *90*, 87-104.

Dixon, J. E., E. M. Stolper, and J. R. Holloway (1995), An Experimental Study of Water and Carbon Dioxide Solubilities in Mid-Ocean Ridge Basaltic Liquids. Part I: Calibration and Solubility Models, *J. Petrology*, *36*, 1607-1631.

Fine, G., and E. Stolper (1986), Dissolved carbon dioxide in basaltic glasses: concentrations and speciation, *Earth and Planetary Science Letters*, *76*, 263-278.

Fornari, D. J. (2003), A new deep-sea towed digital camera and multi-rock coring system, *Eos Transactions AGU*, *84*, 69-76.

Fundis, A., S. Soule, D. Fornari, and M. Perfit (in review), Paving the seafloor: volcanic emplacement processes during the 2005-06 eruption at the fast-spreading East Pacific Rise, 9° 50′N, *Geochemistry, Geophysics, and Geosystems*.

Gaonac'h, H., S. Lovejoy, J. Stix, and D. Scherzter (1996), A scaling growth model for bubbles in basaltic lava flows, *Earth and Planetary Science Letters*, *139*, 395-409.

Goss, A. R., M. R. Perfit, W. I. Ridley, K. H. Rubin, G. D. Kamenov, S. A. Soule, A. Fundis, and D. J. Fornari (2010), Geochemistry of lavas from the 2005-2006 eruption at the East Pacific Rise, 9° 46′N-9°56′N: Implications for ridge crest plumbing and decadal changes in magma chamber compositions, *Geochem. Geophys. Geosyst.*, *11*, Q05T09.

Gregg, T. K. P., D. J. Fornari, M. R. Perfit, R. M. Haymon, and J. H. Fink (1996), Rapid Emplacement of a mid-ocean ridge lava flow on the East Pacific Rise at 9°46′-51′N, *Earth and Planetary Science Letters*, *144*, E1-E7.

Gregg, T. K. P., D. J. Fornari, M. R. Perfit, W. I. Ridley, and M. D. Kurz (2000), Using submarine lava pillars to record mid-ocean ridge eruption dynamics, *Earth and Planetary Science Letters*, *178*, 195-214.

Harding, A. J., G. M. Kent, and J. A. Orcutt (1993), A Multichannel Seismic Investigation of Upper Crustal Structure at 9°N on the East Pacific Rise: Implications for Crustal Accretion, *J. Geophys. Res.*, *98*.

Harris, A. J. L., J. B. Murray, S. E. Aries, M. A. Davies, L. P. Flynn, M. J. Wooster, R. Wright, and D. A. Rothery (2000), Effusion rate trends at Etna and Krafla and their

implications for eruptive mechanisms, *Journal of Volcanology and Geothermal Research*, *102*, 237-269.

Hauri, E., J. Wang, J. E. Dixon, P. L. King, C. Mandeville, and S. Newman (2002), SIMS analysis of volatiles in silicate glasses: 1. Calibration, matrix effects and comparisons with FTIR, *Chemical Geology*, *183*, 99-114.

Haymon, R. M., D. J. Fornari, K. L. Von Damm, M. D. Lilley, M. R. Perfit, J. M. Edmond, W. C. Shanks Iii, R. A. Lutz, J. M. Grebmeier, S. Carbotte, D. Wright, E. McLaughlin, M. Smith, N. Beedle, and E. Olson (1993), Volcanic eruption of the mid-ocean ridge along the East Pacific Rise crest at 9° 45-52' N: Direct submersible observations of seafloor phenomena associated with an eruption event in April, 1991, *Earth and Planetary Science Letters*, *119*, 85-101.

Kent, G. M., A. J. Harding, and J. A. Orcutt (1993), Distribution of Magma Beneath the East Pacific Rise Between the Clipperton Transform and the 9°17′N Deval From Forward Modeling of Common Depth Point Data, *Journal of Geophysical Research*, *98*, 13,945-913,969.

Kurz, M. D., J. Curtice, D. E. Lott, III, and A. Solow (2004), Rapid helium isotopic variability in Mauna Kea shield lavas from the Hawaiian Scientific Drilling Project, *Geochem. Geophys. Geosyst.*, *5*, Q04G14.

Kurz, M. D., and W. J. Jenkins (1981), The distribution of helium in oceanic basalt glasses, *Earth and Planetary Science Letters*, *53*, 41-54.

Le Roux, P. J., S. B. Shirey, E. H. Hauri, M. R. Perfit, and J. F. Bender (2006), The effects of variable sources, processes and contaminants on the composition of northern EPR MORB (8-10°N and 12-14°N): Evidence from volatiles (H_2O, CO_2, S) and halogens (F, Cl), *Earth and Planetary Science Letters*, *251*, 209-231.

Mangan, M. T., K. V. Cashman, and S. Newman (1993), Vesiculation of basaltic magma during eruption, *Geology*, *21*, 157-160.

Marsh, B. D. (1988), Crystal size distribution (CSD) in rocks and the kinetics and dynamics of crystallization, *Contributions to Mineralogy and Petrology*, *99*, 277-291.

Marty, B., and A. Jambon (1987), C/^{3}He in volatile fluxes from the solid Earth: implications for carbon geodynamics, *Earth and Planetary Science Letters*, *83*, 16-26.

Marty, B., and I. N. Tolstikhin (1998), CO_2 fluxes from mid-ocean ridges, arcs and plumes, *Chemical Geology*, *145*, 233-248.

Moore, J. G. (1965), Petrology of deep-sea basalt near Hawaii, *American Journal of Science*, *263*, 40-52.

Moore, J. G., J. N. Batchelder, and C. G. Cunningham (1977), CO_2-Filled Vesicles in Mid-Ocean Basalt, *Journal of Volcanology and Geothermal Research*, *2*, 309-327.

Newman, S., and J. B. Lowenstern (2002), VolatileCalc: a silicate-H_2O-CO_2 solution model written in Visual Basic for Excel, *Computers & Geoscience*, *28*, 597-604.

Paonita, A., and M. Martelli (2007), A new view of the He-Ar-CO_2 degassing at mid-ocean ridges: Homogeneous composition of magmas from the upper mantle, *Geochimica et Cosmochimica Acta*, *71*, 1747-1763.

Prousevitch, A. A., D. L. Sahagian, and A. T. Anderson (1993), Dynamics of Diffusive Bubble Growth in Magmas: Isothermal Case, *Journal of Geophysical Research*, *98*, 22,283-222,307.

Proussevitch, A. A., D. L. Sahagian, and W. D. Carlson (2007), Statistical analysis of bubble and crystal size distributions: Application to Colorado Plateau basalts, *Journal of Volcanology and Geothermal Research*, *164*, 112-126.

Randolph, A. D., and M. A. Larson (1988), *Theory of Particulate Processes*, 251 pp., Academic Press, New York, NY.

Saal, A. E., E. H. Hauri, C. H. Langmuir, and M. R. Perfit (2002), Vapour undersaturation in primitive mid-ocean-ridge basalt and the volatile content of Earth's upper mantle, *Nature*, *419*, 451-455.

Sarda, P., and D. Graham (1990), Mid-ocean ridge popping rocks: implications for degassing at ridge crests, *Earth and Planetary Science Letters*, *97*, 268-289.

Shaw, A. M., M. D. Behn, S. E. Humphris, R. A. Sohn, and P. M. Gregg (2010), Deep pooling of low degree melts and volatile fluxes at the 85°E segment of the Gakkel Ridge: Evidence from olivine-hosted melt inclusions and glasses, *Earth and Planetary Science Letters*, *289*, 311-322.

Simons, K., J. Dixon, J.-G. Schilling, R. Kingsley, and R. Poreda (2002), Volatiles in basaltic glasses from the Easter-Salas y Gomez Seamount Chain and Easter Microplate: Implications for geochemical cycling of volatile elements, *Geochemistry, Geophysics, and Geosystems*, *3*.

Sinton, J. M., and R. S. Detrick (1992), Mid-Ocean Ridge Magma Chambers, *Journal of Geophysical Research*, *97*, 197-216.

Smith, M. C., M. R. Perfit, D. J. Fornari, W. I. Ridley, M. H. Edwards, G. J. Kurras, and K. L. Von Damm (2001), Magmatic processes and segmentation at a fast spreading mid-ocean ridge: Detailed investigation of an axial discontinuity on the East Pacific Rise crest at 9°37′N, *Geochem. Geophys. Geosyst.*, *2*.

Soule, S. A., D. J. Fornari, M. R. Perfit, and K. H. Rubin (2007), New Insights into mid-ocean ridge volcanic processes from the 2005-2006 eruption of the East Pacific Rise, 9°46′N - 9°56′N, *Geological Society of America*, *35*, 1079-1082.

Sparks, R. S. J. (1978), The dynamics of bubble formation and growth in magmas: A review and analysis, *Journal of Volcanology and Geothermal Research*, *3*, 1-37.

Standish, J. J., H. J. B. Dick, P. J. Michael, W. G. Melson, and T. O'Hearn (2008), MORB generation beneath the ultraslow spreading Southwest Indian Ridge (9-25° E): Major element chemistry and the importance of process versus source, *Geochem. Geophys. Geosyst.*, *9*, Q05004.

Sun, S. S., and W. F. McDonough (1989), Chemical and isotopic systematics of oceanic basalts: implications for mantle composition and processes, *Geological Society, London, Special Publications*, *42*, 313-345.

Tolstoy, M., J. P. Cowen, E. T. Baker, D. J. Fornari, K. H. Rubin, T. M. Shank, F. Waldhauser, D. R. Bohnenstiehl, D. W. Forsyth, R. C. Holmes, B. Love, M. R. Perfit, R. T. Weekly, S. A. Soule, and B. Glazer (2006), A Seafloor Spreading Event Captured by Seismometers, *Science*, *314*, 1920-1922.

Toomey, D. R., G. M. Purdy, S. C. Solomon, and W. S. D. Wilcock (1990), The three-dimensional seismic velocity structure of the East Pacific Rise near latitude 9° 30′ N, *Nature*, *347*, 639-645.

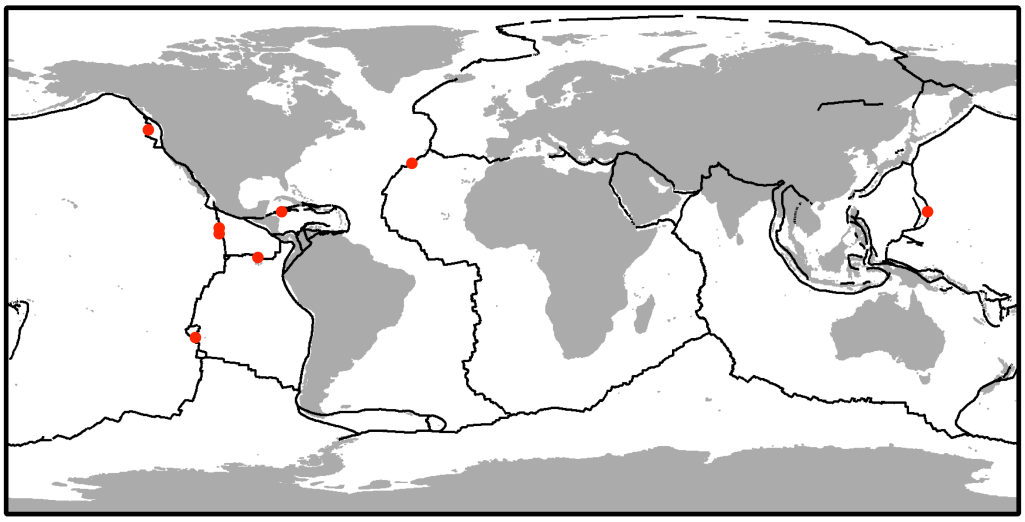

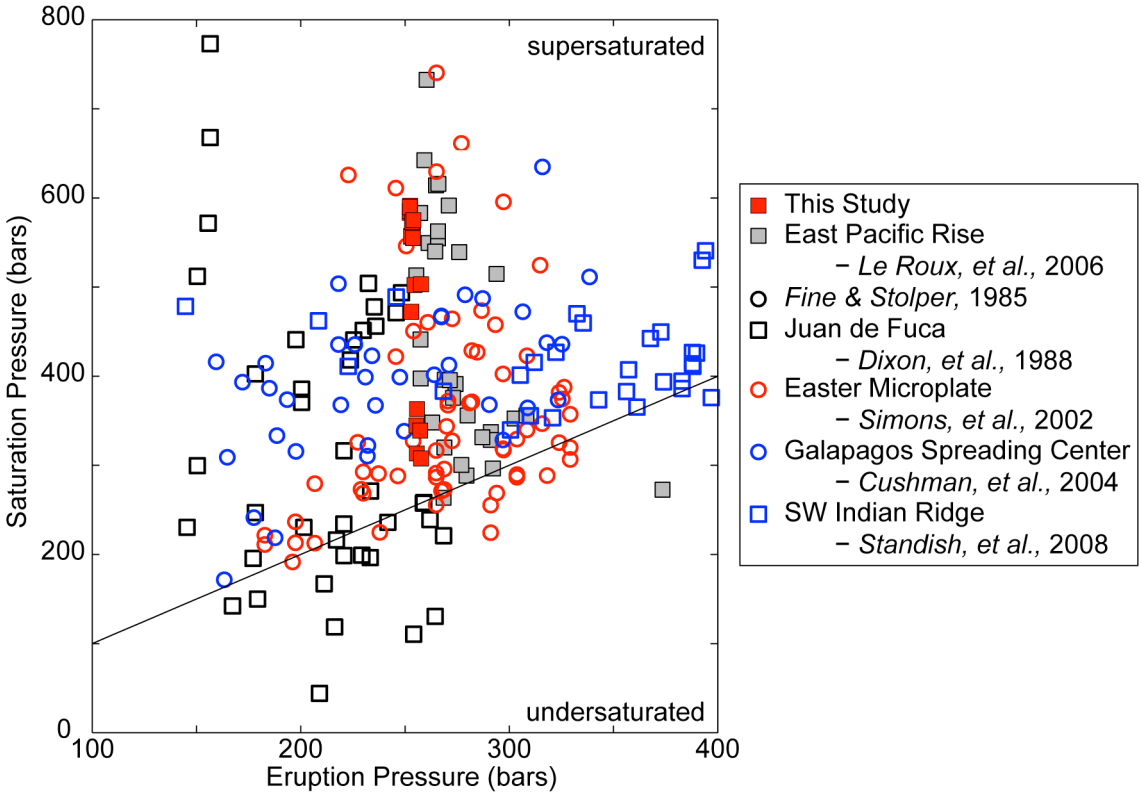
800
600
400
200
0
100
200
300
400
Saturation Pressure (bars)
Eruption Pressure (bars)
supersaturated
undersaturated
This Study
East Pacific Rise
− Le Roux, et al., 2006
Fine & Stolper, 1985
Juan de Fuca
− Dixon, et al., 1988
Easter Microplate
− Simons, et al., 2002
Galapagos Spreading Center
− Cushman, et al., 2004
SW Indian Ridge
− Standish, et al., 2008

Figure 1. (*Map*) Location map of areas for which dissolved CO_2 and H_2O measurements in MORB are available including: the Juan de Fuca Ridge, East Pacific Rise, Easter Microplate, Galapagos Spreading Center, Cayman Trough, Mid Atlantic Ridge (FAMOUS), Marianas Trench, and Southwest Indian Ridge. (*Plot*) Equilibrium saturation pressure vs. eruption pressure for global MORB glass samples and from *Jason II* samples used in this study (red squares). Equilibrium saturation pressures are calculated from VolatileCalc (*Newman & Lowenstern,* 2002, based on *Dixon,* 1995 and *Dixon, et al.,* 1995) using measured dissolved CO_2 and H_2O concentrations; eruption pressures are calculated from the recorded seafloor depth of each sample. If in saturation equilibrium with their ambient seafloor pressures, samples should fall along the 1:1 line indicated in black. Instead, volatile concentrations indicate that MORBs exhibit varying degrees of saturation to supersaturation, and rarely undersaturation, relative to their eruption depths. This disequilibrium indicates that melts are not fully degassed during ascent, as would be predicted by Henry's Law.

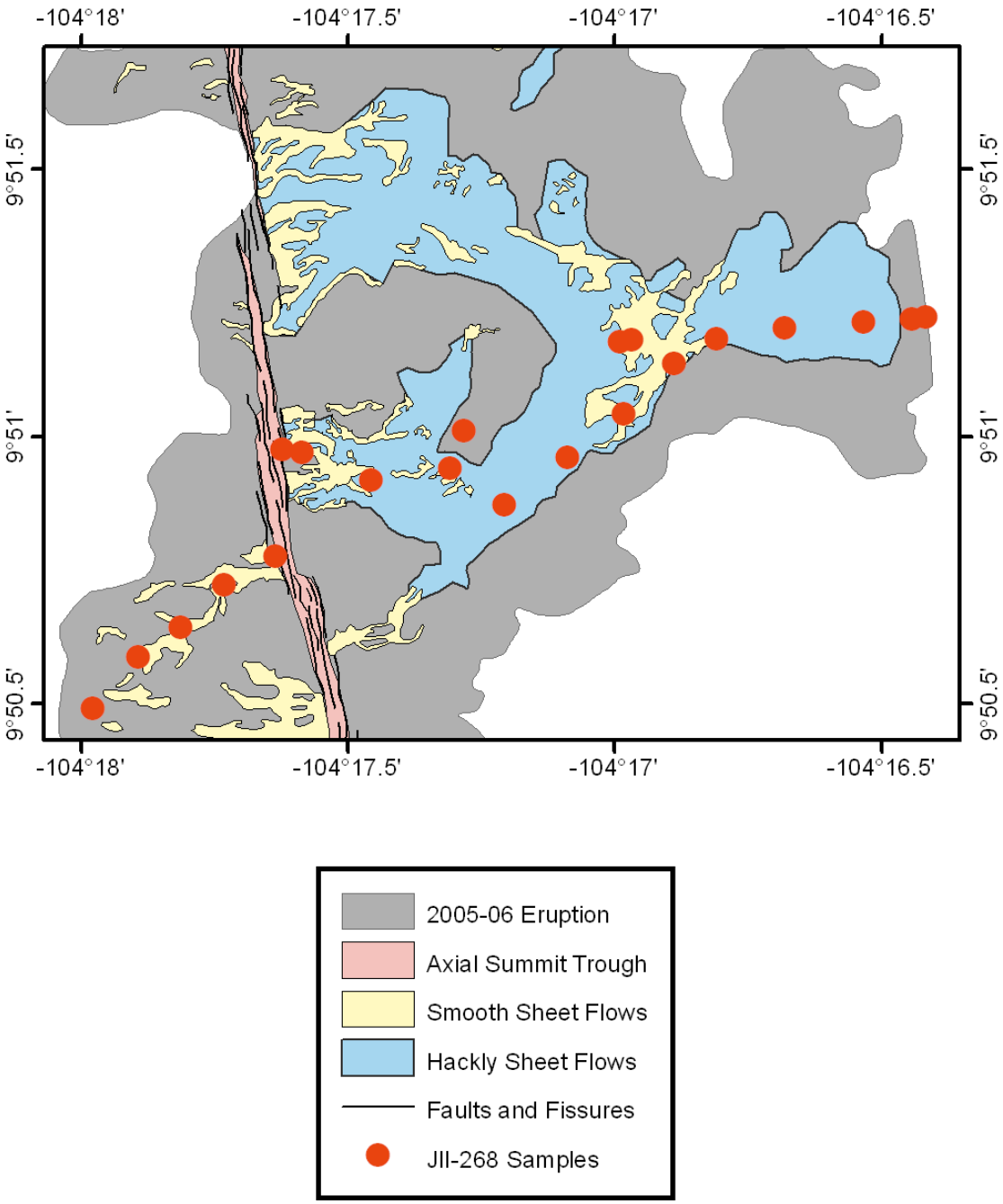
-104°18'
-104°17.5'
-104°17'
-104°16.5'
9°51.5'
9°51'
9°50.5'
2005-06 Eruption
Axial Summit Trough
Smooth Sheet Flows
Hackly Sheet Flows
Faults and Fissures
JII-268 Samples

Figure 2. Interpretive map of the 9° 51′ N flow lobe area, based on sidescan sonar imagery and seafloor photos from cruise AT15-17 (April 2007). The EPR axial summit trough (red) is thought to be the flow source for the 2005-06 lavas. Sheet (yellow) and hackly (blue) flow morphologies, which were used to identify this single flow path, are shown relative to the extent of the 2005-06 flow (gray). Location of MORB glass samples from this single flow path, collected by *Jason II* (Dive 268), are shown by red markers. Samples were collected at ~200 m intervals, and thus record the geochemical and physical changes in the melt over the length (and therefore time) of the eruption. *Mapping of flow morphology by S.A. Soule.*

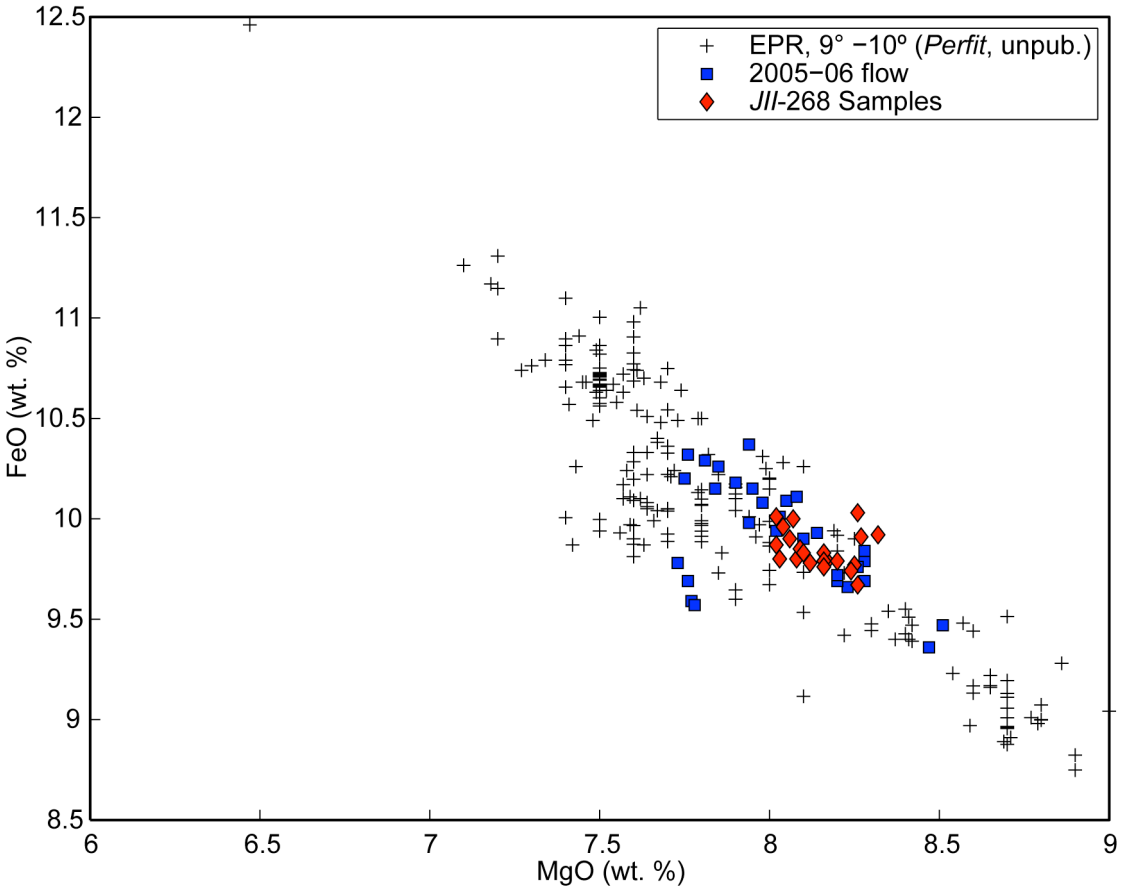

Figure 3. FeO vs. MgO content of MORB glasses from the 9° 51´ N flow lobe (red) [*Goss, et al.,* 2010], relative to other samples from the 2005-06 eruption (blue) and the large-scale variability of the EPR, 9° -10° N (black) [*Perfit*, unpublished data]. Homogeneity of the *JII*-268 samples indicates that differentiation of the flow did not occur during emplacement. Crystallization of olivine or plagioclase would result in a systematic increase in FeO with decreasing MgO content.

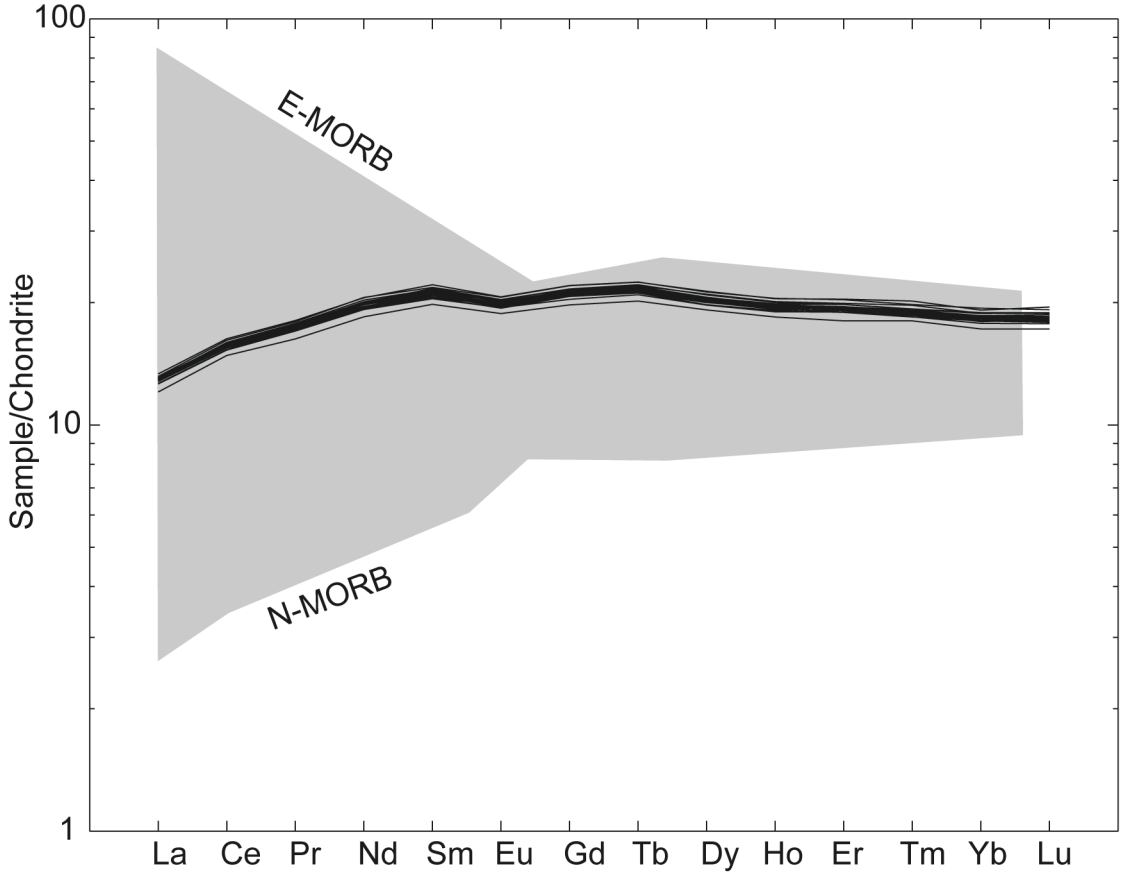

Figure 4. Rare earth elements (REEs) of *JII*-268 MORB glass samples, normalized to chondritic concentrations [*Sun & McDonough*, 1989]; REE patterns are shown relative to the range of E-MORB and N-MORB (gray) [*Wilson,* 1989]. Relative concentrations are typical of N-MORB trace element patterns, with depleted light REEs and flat middle to heavy REEs. Homogeneous concentrations between samples, particularly in the more incompatible light REEs which would increase during crystallization, supports that the *JII*-268 suite represent products from a single parent magma. *Trace element analysis performed by AT Fundis.*

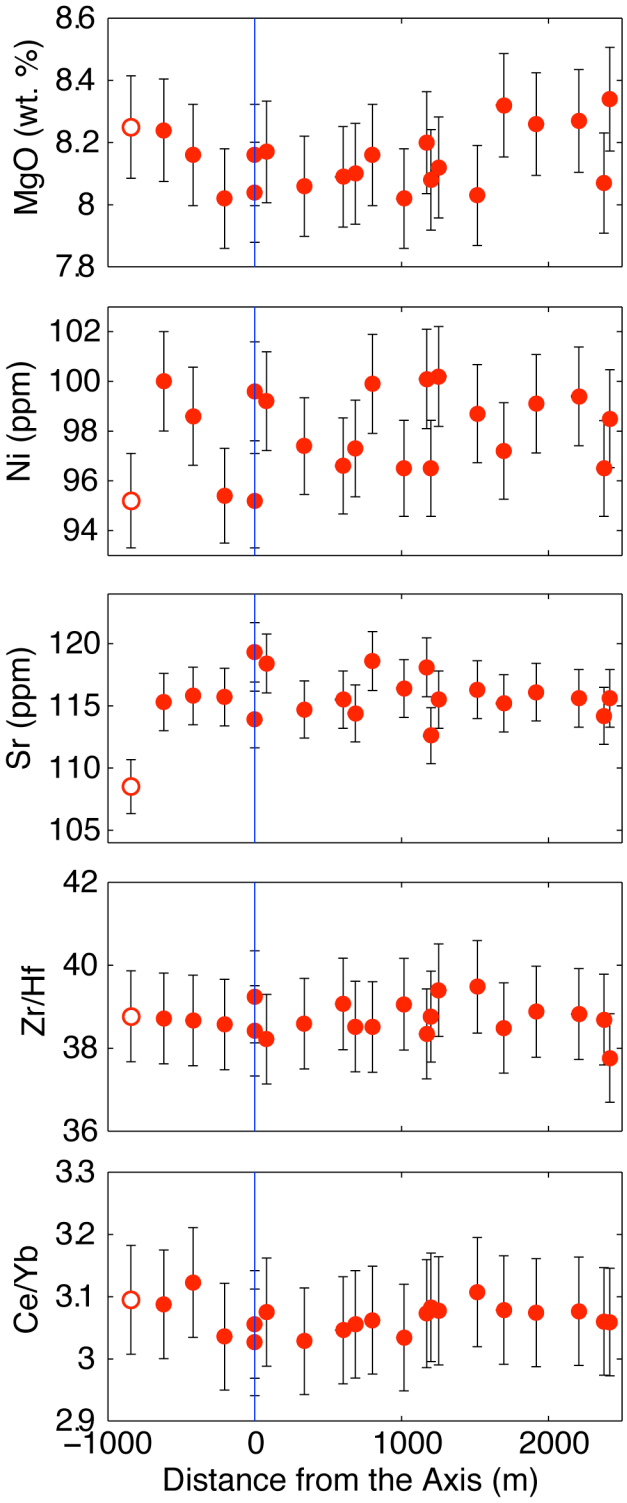
MgO (wt. %)
8.6
8.4
8.2
8
7.8
Ni (ppm)
102
100
98
96
94
Sr (ppm)
120
115
110
105
Zr/Hf
42
40
38
36
Ce/Yb
3.3
3.2
3.1
3
2.9
−1000
0
1000
2000
Distance from the Axis (m)

Figure 5. Concentrations of MgO, Ni, selected trace elements, and selected trace element ratios vs. distance from the axis (positive values indicate meters to the east). Changes in element concentrations and ratios are used to evaluate geochemical variability of the *JII*-268 suite. MgO provides an index of differentiation of the melt, and should decrease with the crystallization of olivine and plagioclase. Ni is compatible in olivine, and should therefore decrease during crystallization of this phase. Sr substitutes for Ca in plagioclase, and will also decrease with crystallization. Zr and Hf are both compatible in zircon and incompatible in silicate phases; Zr/Hf ratio may be used to assess mantle melting processes, as well as crystallization during emplacement; this ratio should increase with crystallization as Zr becomes more concentrated in the melt. Ce is a highly incompatible light rare earth element (REE), whereas Yb is a compatible heavy REE; during crystallization, Ce would become enriched relative to Yb concentrations and result in an increase in Ce/Yb. All trends indicate uniform compositions throughout the flow, with the exception of sample *JII*-268-01 (open red circle, ~843 m west of the axis). This sample exhibits a distinct composition, as shown in plots of Ni and Sr; the sample was collected at the western terminus of the flow, where eruption boundaries are difficult to determine, and may therefore represent the product of a different/older flow. Lack of statistically significant variations in geochemistry suggest that fractional crystallization did not occur during emplacement, and thus that the lava flow was isothermal. *Trace element analysis by AT Fundis.*

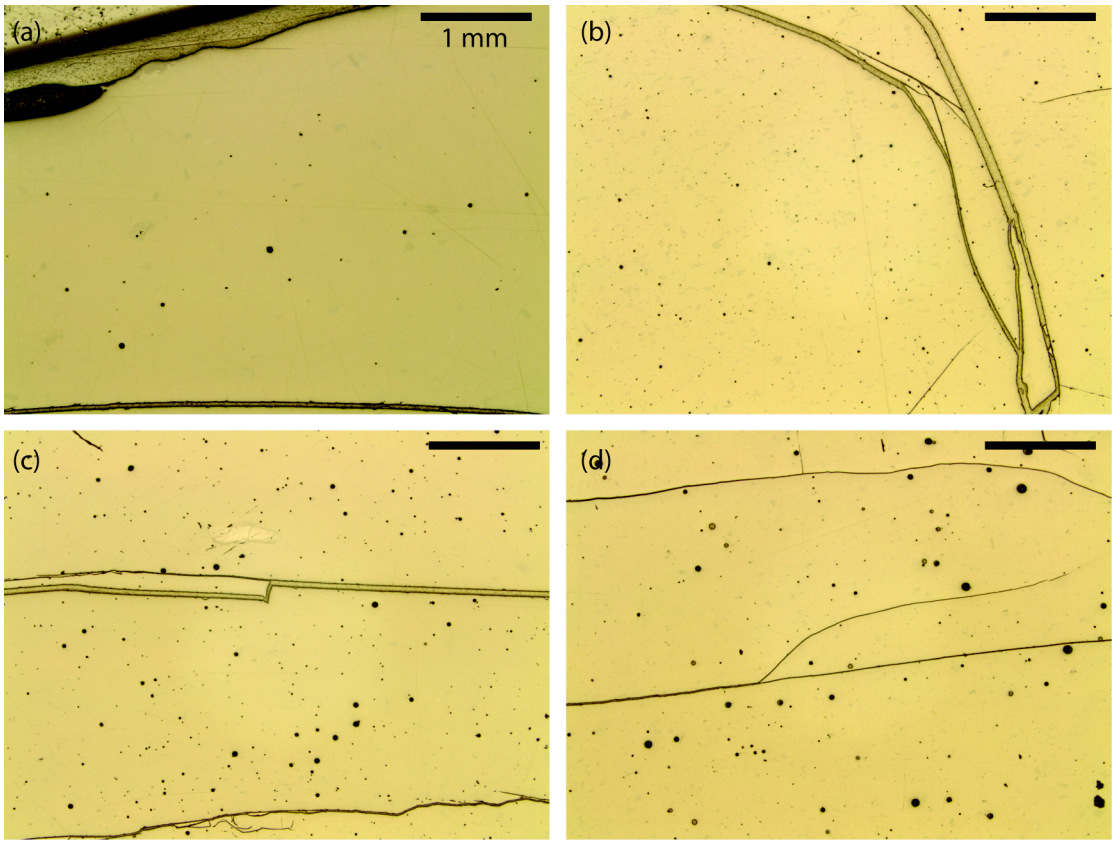

Figure 6. Reflected light images of MORB glass thin sections at 2.5x magnification of (a) *JII*-268-10 at the axis, (b) *JII*-268-13 within ~1 km of the axis, (c) *JII*-268-18 in the transition zone of decreasing CO_2, and (d) *JII*-268-23 off axis. 1-mm bar given for scale. Vesicularity increases ~1% over the ~2.5 km of lateral flow.

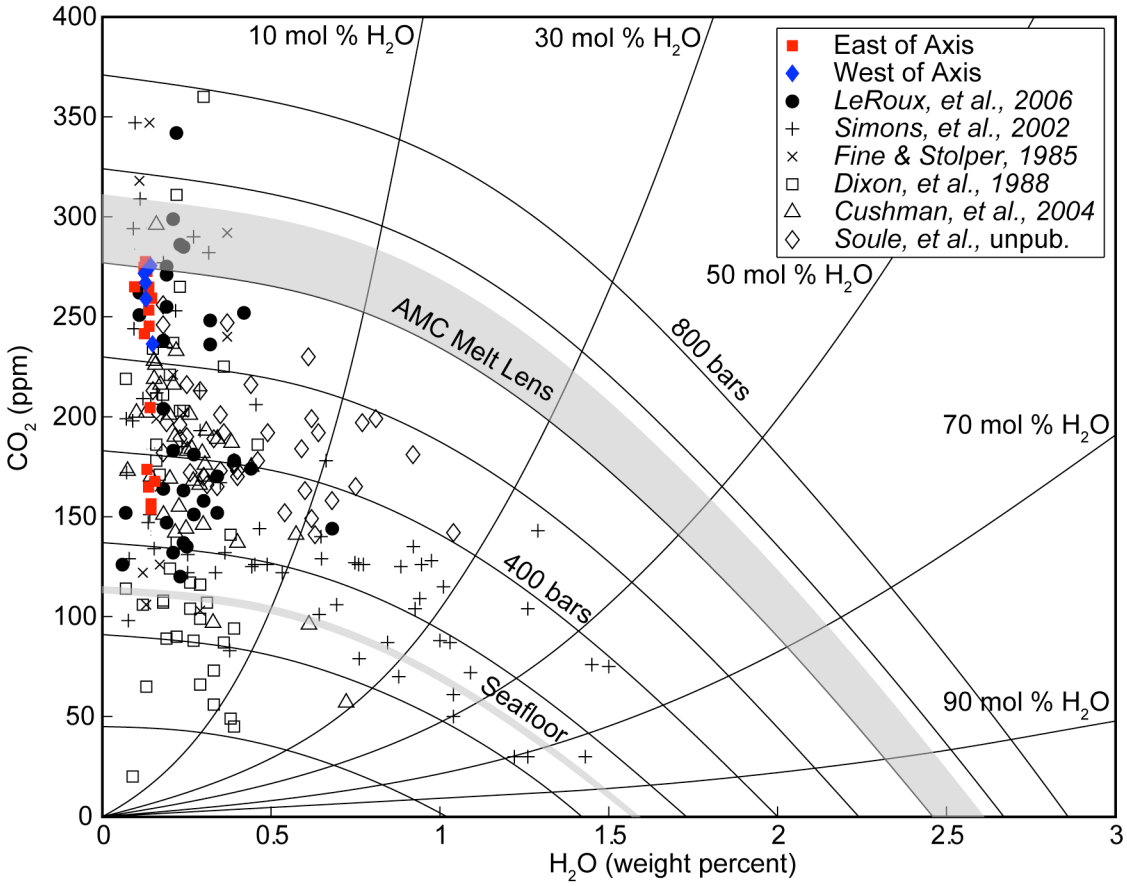

Figure 7. CO_2 (ppm) vs. H_2O (weight percent) for EPR 9-10° N samples. CO_2 concentrations from the 2005-06 flow (this study) range from154-278 ppm, and span a large portion of the variability exhibited by MORBs from the EPR (black circles) [*Le Roux et al., 2006*] and globally. H_2O concentrations for this study range from 0.10-0.16, and do not vary significantly compared to EPR and global MORB measurements. Solid lines are curves of constant pressure and constant vapor composition based on Volatile Calc [*Newman & Lowenstern*, 2002]. The shaded region between ~600 and 670 bars corresponds to the approximate location of the axial magma chamber, ~1250-1500 mbsf. The shaded region between 246-252 bars is consistent with seafloor depths of 2503-2558 mbsl. CO_2 content of the erupted magma indicates initial near equilibrium with the magma chamber (i.e. supersaturation with respect to the seafloor). CO_2-pressure equilibrium is nearly achieved through degassing during emplacement for the 2005-06 flow.

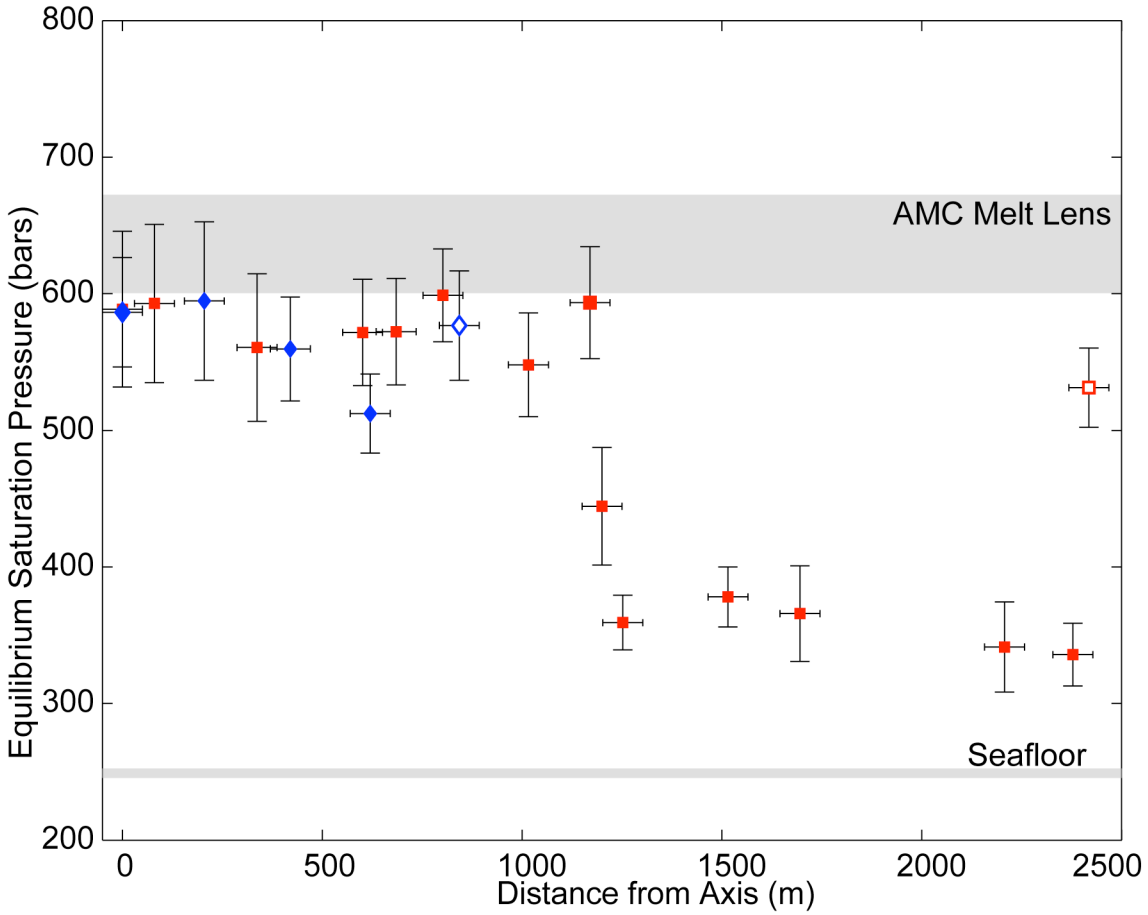

Figure 8. Equilibrium saturation pressure vs. distance from the axis. Equilibrium saturation pressures are calculated from dissolved CO_2 and H_2O concentrations in the melt [*Dixon*, 1995a; *Dixon, et al.*, 1995; *Newman and Lowenstern*, 2002]. Shaded regions correspond to the depth of the axial magma chamber melt lens at ~1250-1500 mbsf and seafloor depths of 2503-2558 mbsl. Based on side scan sonar analysis and flow morphology, *JII*-268-24 (open red square, ~2418 m from vent) may differ in dynamics or source. In addition, *JII*-268-01 (open blue diamond, ~843 m from the axis) exhibits a distinct trace element signature (see text). These two samples were collected from the termini of the flow where identification of eruption boundaries are difficult, and may therefore represent the products of other flow paths.

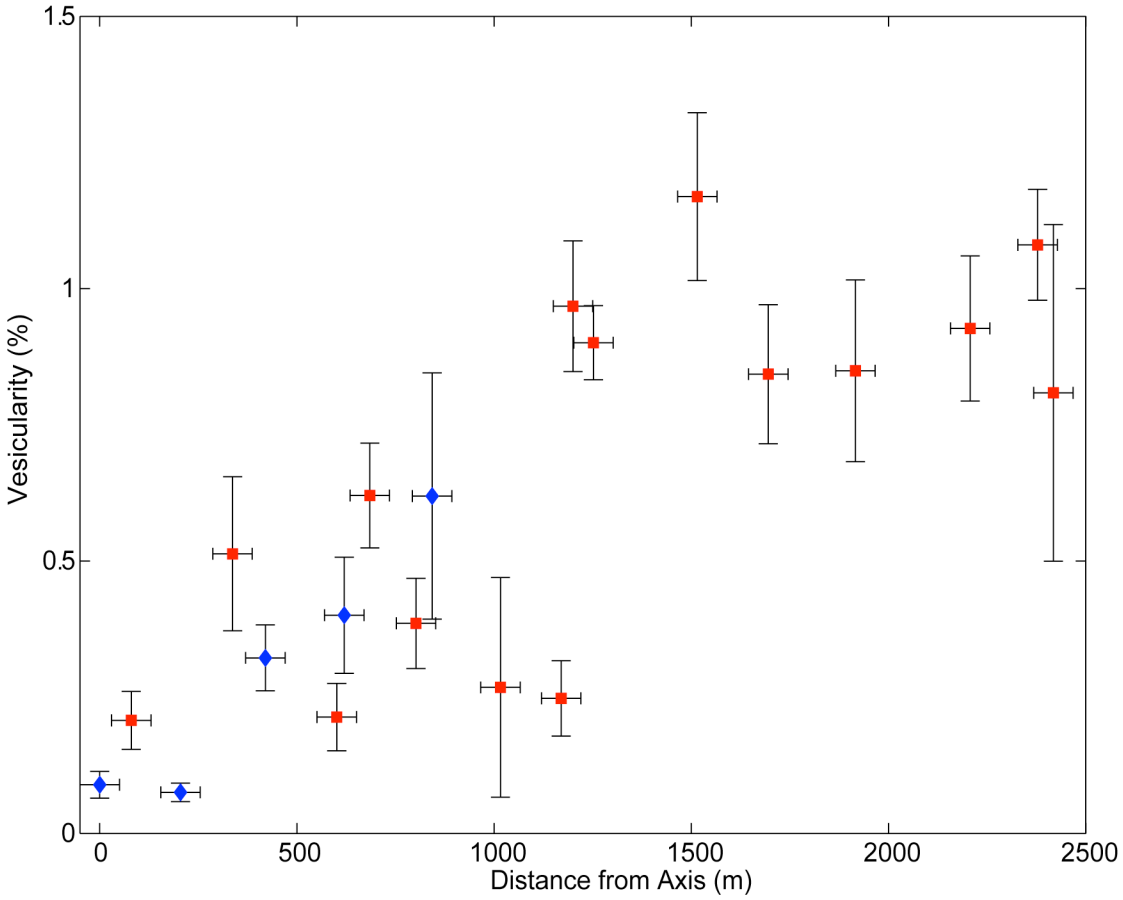

Figure 9. Vesicularity vs. distance from the axis. Vesicularity ranges from ~0.1-1.2 % and is measured from images of MORB glass thin sections. The scale of increase in vesicularity is within the range predicted by CO_2 lost as an ideal gas. This increase reflects the increasing CO_2 vapor volume as CO_2 exsolves from the melt, and indicates that neither vesicles nor total volatile content are lost from the flow during emplacement.

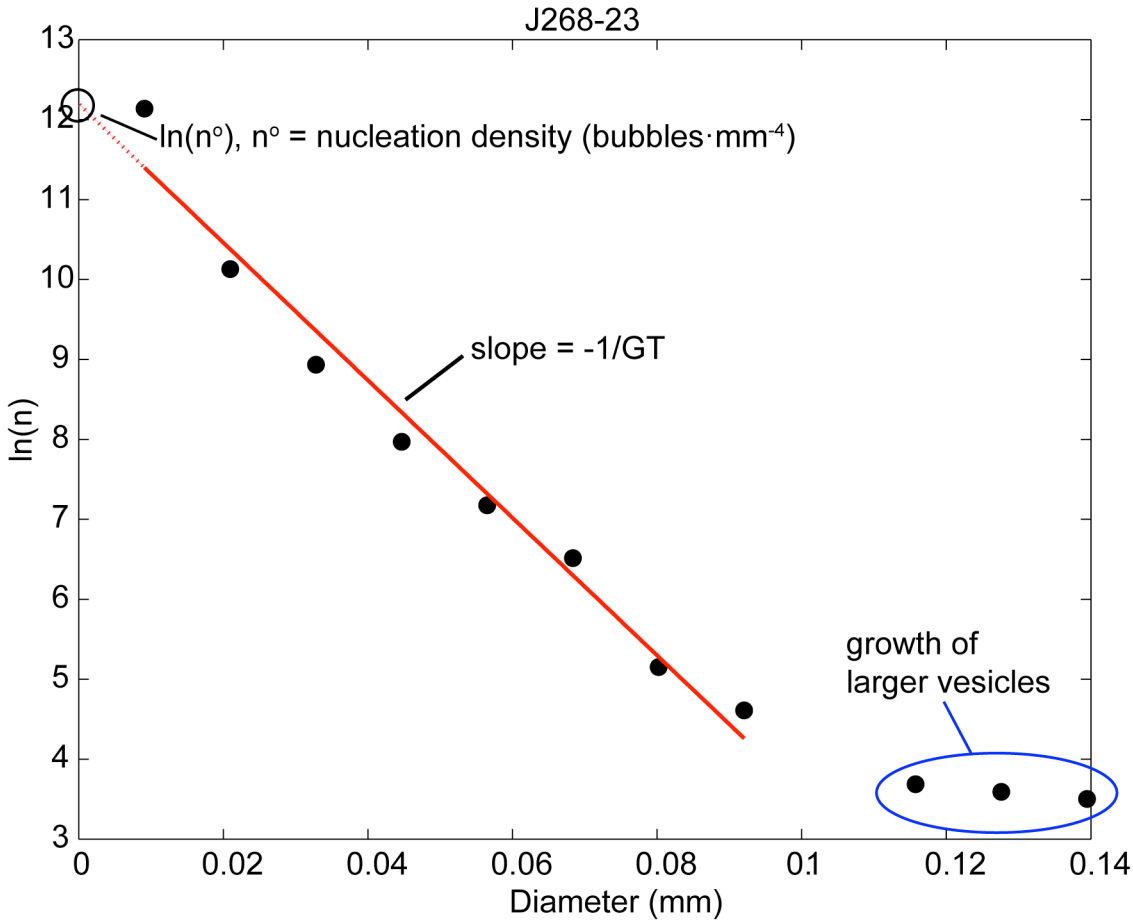

Figure 10. Example of ln *n* vs. *L* plot for *JII*-268-23, located ~2378 m off-axis at the eastern termini of the flow path. The slope is used to calculate $G\tau$ and the y-intercept is used to calculate $n°$, the volumetric nuclei density. These values are subsequently used to calculate vesicle size and vesicle density in a 3-D volume of melt, as well as evaluate vesicle growth rate (G), eruption duration (τ), and flow rate. It is typical for such plots to deviate from linearity at larger vesicle sizes due to processes such as bubble coalescence or a population of larger, inherited, pre-eruption vesicles.

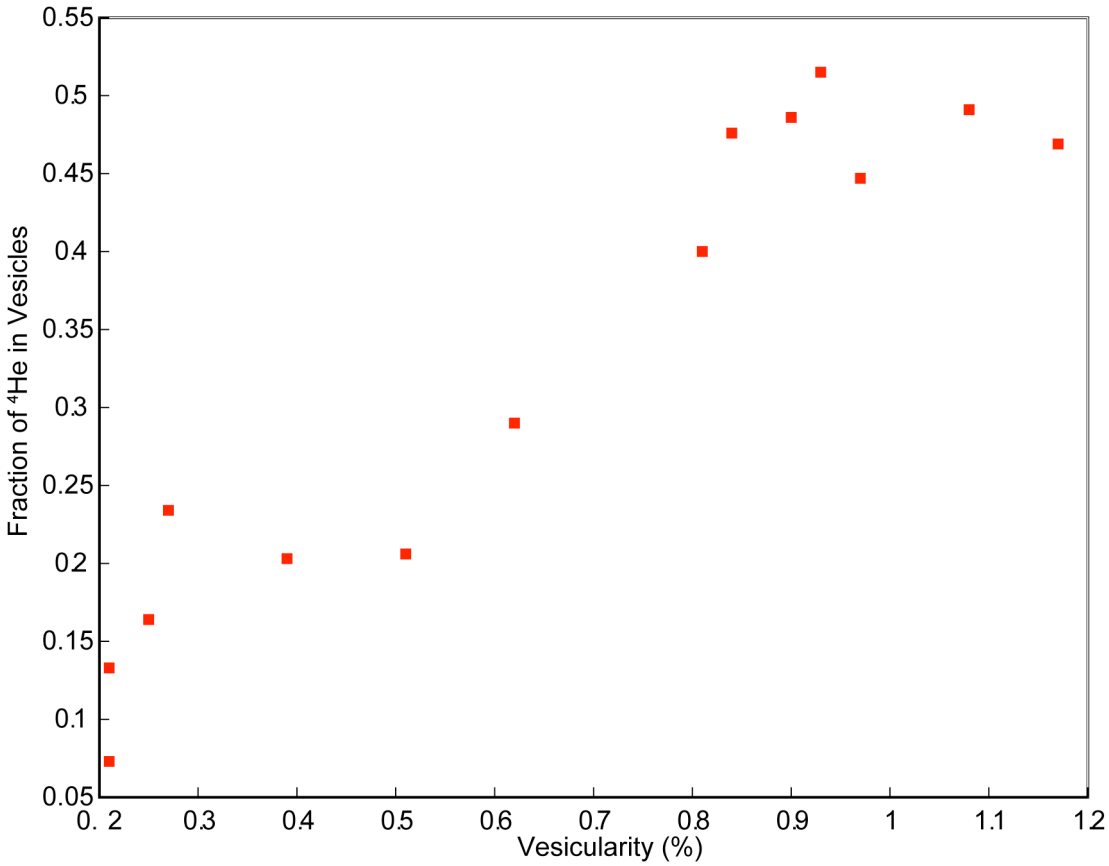

Figure 11. Fraction of ^{4}He in vesicles vs. vesicularity for *JII*-268 samples east of the vent. This increase reflects the partitioning of He into vesicles as CO_2 exsolves into an increasing vapor (vesicle) volume over the length of the flow.

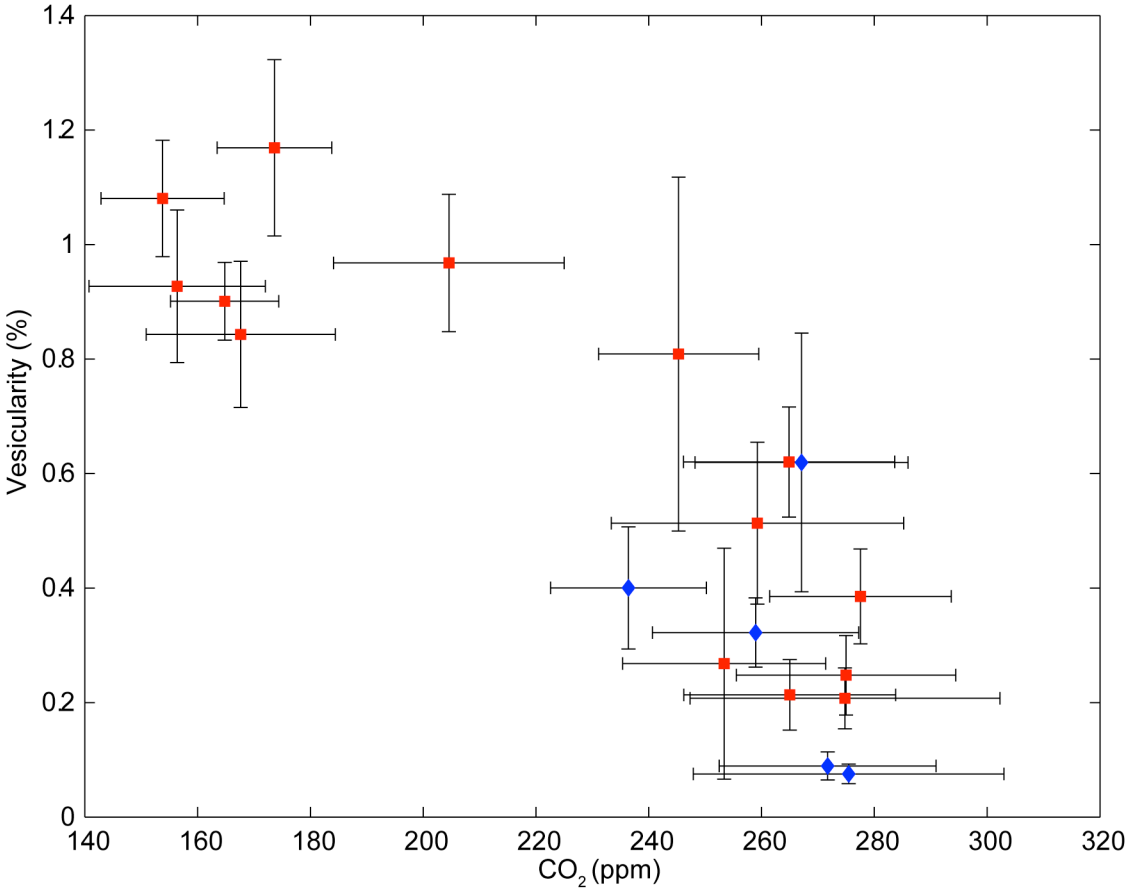

Figure 12. Vesicularity vs. dissolved CO_2 in the melt. As CO_2 decreases in the melt and increases in the vapor phase, vesicularity increases; this indicates that CO_2 lost from the melt is accommodated by growth in vesicle size or number, and that neither vesicles nor CO_2 are lost from the flow.

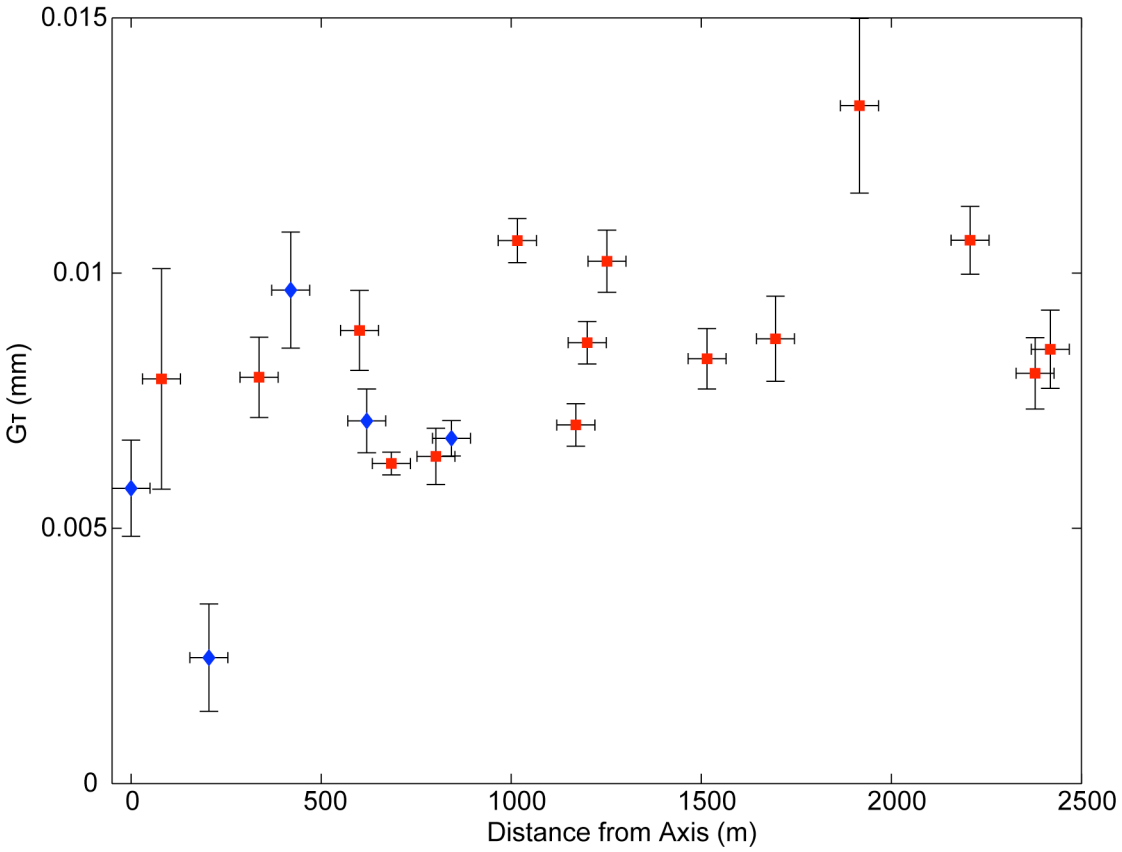

Figure 13. Growth rate × duration of vesicle growth, Gτ, versus distance from the axis. Gτ also provides an approximation for the dominant vesicle diameter, L_D. There is a weak increase in dominant vesicle size over the length of the 2005-06 eruption. This increase (and the lack of a systematic trend in vesicle density) suggests that diffusion of CO_2, rather than nucleation of new vesicles, is a dominant processes in accommodating the increasing vapor volume shown by increasing vesicularity over distance.

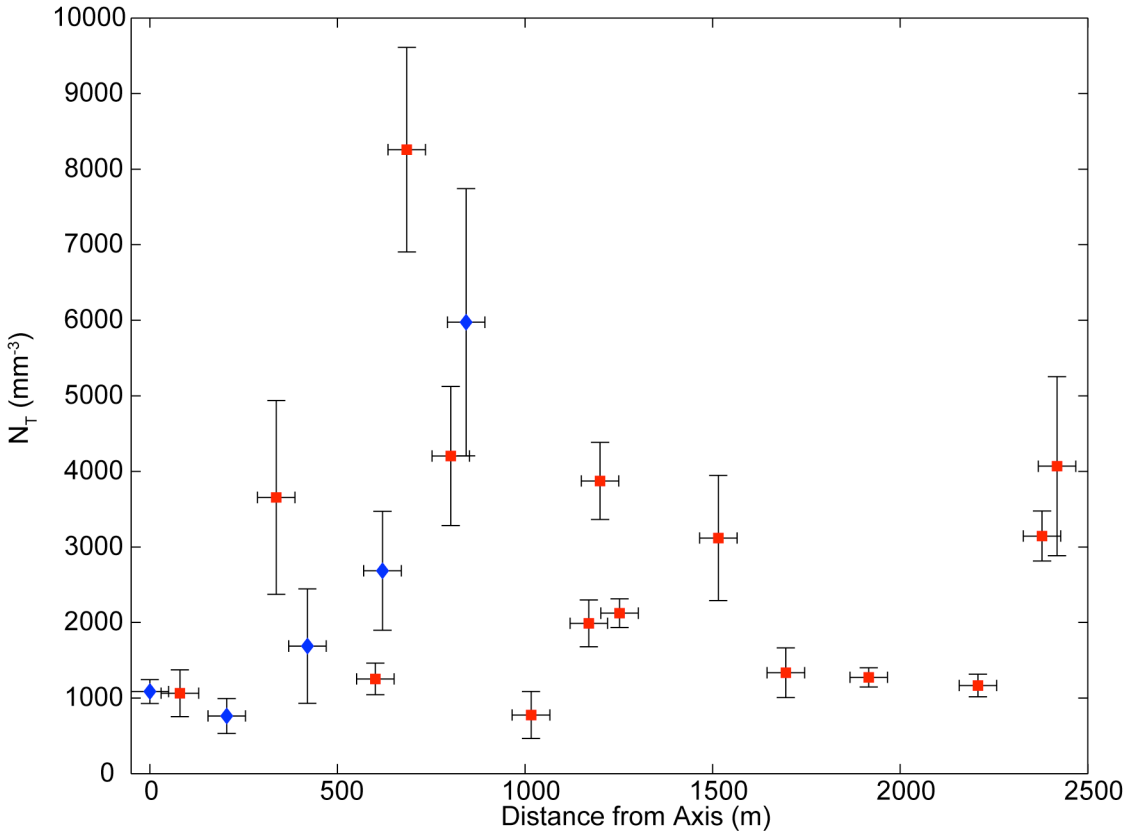

Figure 14. 3-D Vesicle density, N_T, vs. distance from the axis. $N_T = n^o G\tau$. There is no statistically significant change in vesicle density over the length of the 2005-06 eruption. This indicates that nucleation, which would result in an increase in vesicle density, and coalescence and Ostwald ripening, which would result in decreases in vesicle density, are likely not altering the vesicle population during emplacement.

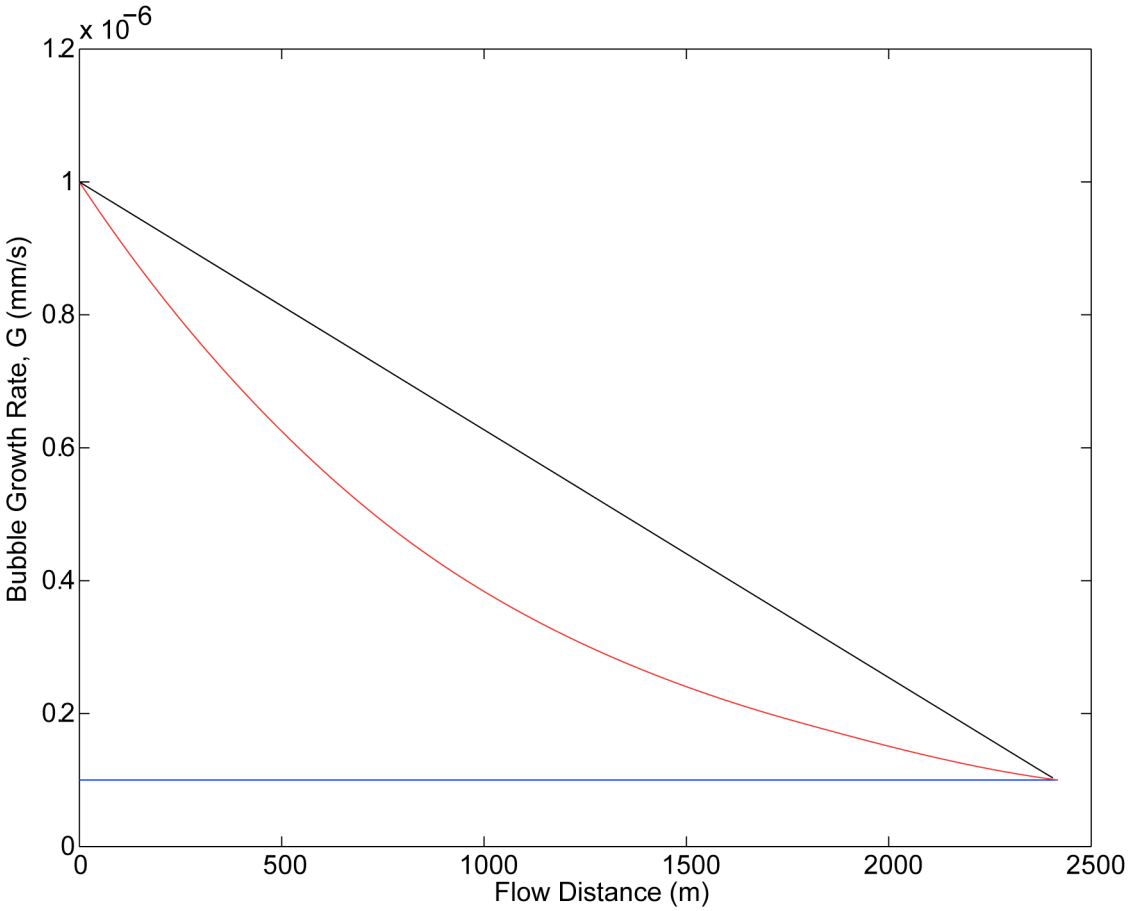

Figure 15. Growth rate models used to constrain eruption duration and velocity: (1) constant growth rate of 1 x 10^{-7} mm/s in blue, (2) linearly decreasing growth rate, from 1 x 10^{-6} -1 x 10^{-7} mm/s, in black, and (3) exponentially decreasing growth rate, from 1 x 10^{-6} -1 x 10^{-7} mm/s, in red. Models of decreasing growth rate are more realistic, as they account for the decreasing chemical gradient of CO_2, decreasing degree of volatile supersaturation, and the approach of vesicles toward their final sizes with increasing vapor volume.

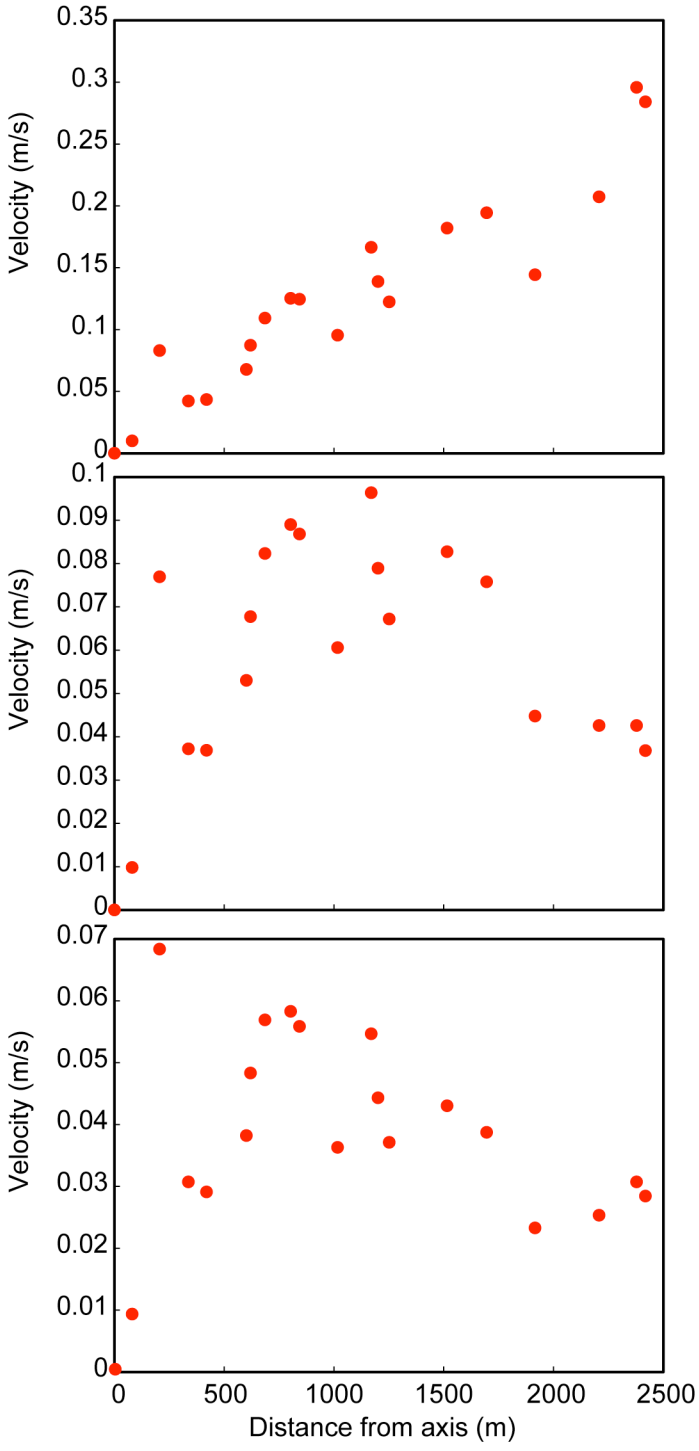
Velocity (m/s)
0.35
0.3
0.25
0.2
0.15
0.1
0.05
0
Velocity (m/s)
0.1
0.09
0.08
0.07
0.06
0.05
0.04
0.03
0.02
0.01
0
Velocity (m/s)
0.07
0.06
0.05
0.04
0.03
0.02
0.01
0
0
500
1000
1500
2000
2500
Distance from axis (m)

Figure 16. Velocity profiles resulting from a constant vesicle growth rate (top), linearly decreasing vesicle growth rate (middle), and exponentially decreasing growth rate (bottom). Total emplacement times are 3.7 hrs, 18 hrs, and 24 hrs, respectively for each of the velocity profiles above. A constant vesicle growth rate results in an unrealistic velocity profile, with lava advance rate increasing over the length of the flow. Linearly decreasing and exponentially decreasing vesicle growth models more accurately reflect actual lava advance rates, which should decrease as lava advance comes to a stop. Based on decreasing vesicle growth rates, we estimate lava advance rates of 0.01-0.1 m/s.

Table 1. Location of MORB glasses from 2005-06 eruption.

Sample	Lon. (West)	Lat. (North)	Depth (m)	Axial Distance (m)
JII-268-1	104°17.98′	9°50.49′	2519	843
JII-268-2	104°17.89′	9°50.59′	2512	620
JII-268-3	104°17.81′	9°50.64′	2511	420
JII-268-4	104°17.73′	9°50.72′	2506	205
JII-268-5	104°17.64′	9°50.78′	2504	0
JII-268-9	104°17.62′	9°50.97′	2503	0
JII-268-10	104°17.58′	9°50.97′	2504	80
JII-268-11	104°17.46′	9°50.92′	2511	337
JII-268-12	104°17.31′	9°50.94′	2515	601
JII-268-13	104°17.28′	9°51.01′	2519	685
JII-268-14	104°17.21′	9°50.87′	2522	802
JII-268-15	104°17.09′	9°50.96′	2527	1016
JII-268-16	104°16.98′	9°51.04′	2532	1170
JII-268-17	104°16.97′	9°51.18′	2536	1252
JII-268-18	104°16.99′	9°51.18′	2533	1200
JII-268-19	104°16.89′	9°51.14′	2538	1515
JII-268-20	104°16.81′	9°51.18′	2539	1695
JII-268-22	104°16.53′	9°51.21′	2554	2207
JII-268-23	104°16.42′	9°51.22′	2558	2378
JII-268-24	104°16.44′	9°51.22′	2558	2418

Table 2. Volatile concentrations in *JII*-268 MORB glass.

Sample	CO_2 (ppm)	H_2O (wt. %)	F (ppm)	S (ppm)	Cl (ppm)
JII-268-1	267	0.13	111	1043	64
JII-268-2	236	0.15	113	1087	71
JII-268-3	259	0.13	106	1120	66
JII-268-4	275	0.14	110	1119	68
JII-268-5	272	0.12	110	1128	68
JII-268-9	273	0.13	108	1132	67
JII-268-10	275	0.12	101	1099	61
JII-268-11	259	0.15	110	1153	67
JII-268-12	265	0.10	95	1063	62
JII-268-13	265	0.14	115	1090	69
JII-268-14	278	0.13	109	1119	65
JII-268-15	253	0.14	116	1106	68
JII-268-16	275	0.13	112	1076	70
JII-268-17	165	0.14	111	1124	70
JII-268-18	205	0.14	127	1076	74
JII-268-19	174	0.13	114	1061	9
JII-268-20	168	0.16	110	1153	68
JII-268-22	156	0.14	105	1116	75
JII-268-23	154	0.14	108	1023	81
JII-268-24	245	0.14	104	1084	65

*Analytical uncertainties are ± 10%.

Table 3. Parameters and values used to determine equilibrium saturation pressures and depths*.

Parameter	Definition	Value
$X^{m}_{H_2O,mol}$	molar concentration of H_2O in melt	
$X^{o,m}_{H_2O,mol}$	molar concentration of H_2O in melt at (P_0, T_0)	3.28×10^{-3}
$X^{m}_{CO_3^{2-},mol}$	molar concentration of CO_2 in melt	
$X^{o,m}_{CO_3^{2-},mol}$	molar concentration of CO_2 in melt at (P_0,T_0)	3.8×10^{-7}
f_{H_2O}	fugacity of H_2O	
$f_{H_2O}(P_0,T_0)$	fugacity of H_2O at (P_0,T_0)	1 bar
f_{CO_2}	fugacity of CO_2	
$f_{CO_2}(P_0,T_0)$	fugacity of CO_2 at (P_0,T_0)	1 bar
$V^{o.m}_{H_2O}$	molar volume of H_2O in melt at standard conditions	12 cm^3/ mol
$V^{o.m}_{r}$	molar volume of CO_2 in melt at standard conditions	23 cm^3/ mol
P	pressure of melt	
P_0	pressure of melt, initial	1 bar
T_0	temperature (isothermal)	1473 K
R	gas constant	83.15 cm^3 bar/ mol K

*Parameters and values from *Dixon* [1995] and *Newman and Lowenstern* [2002].

Table 4. Equilibrium saturation pressures and depths.

Sample	Equilibrium Pressure (bars)	Equilibrium Depth (m)
JII-268-1	577	1147
JII-268-2	512	920
JII-268-3	560	1086
JII-268-4	595	1210
JII-268-5	586	1181
JII-268-9	589	1188
JII-268-10	593	1203
JII-268-11	561	1090
JII-268-12	572	1129
JII-268-13	572	1131
JII-268-14	599	1224
JII-268-15	548	1045
JII-268-16	593	1205
JII-268-17	359	381
JII-268-18	444	681
JII-268-19	378	447
JII-268-20	366	404
JII-268-22	341	318
JII-268-23	336	299
JII-268-24	531	986

Table 5. 2-D vesicle analysis from thin sections.

Sample	Vesicularity (%)			Vesicle Density (mm^{-2})		
JII-268-1	0.62	±	0.23	41	±	21
JII-268-2	0.40	±	0.11	20	±	10
JII-268-3	0.32	±	0.06	14	±	8
JII-268-4	0.08	±	0.02	5	±	1
JII-268-5	0.09	±	0.02	6	±	1
JII-268-9		--			--	
JII-268-10	0.21	±	0.05	8	±	3
JII-268-11	0.51	±	0.14	27	±	14
JII-268-12	0.21	±	0.06	10	±	2
JII-268-13	0.62	±	0.10	52	±	13
JII-268-14	0.39	±	0.08	28	±	9
JII-268-15	0.27	±	0.20	8	±	5
JII-268-16	0.25	±	0.07	15	±	3
JII-268-17	0.90	±	0.07	22	±	3
JII-268-18	0.97	±	0.12	33	±	5
JII-268-19	1.17	±	0.15	29	±	11
JII-268-20	0.84	±	0.13	14	±	4
JII-268-22	0.93	±	0.13	14	±	2
JII-268-23	1.08	±	0.10	29	±	4
JII-268-24	0.81	±	0.31	33	±	14

Table 6. 3-D Vesicle size distribution.

Sample	$G\tau$ (x 10^{-3} mm)	n^o (x 10^5 mm^{-4})	N_T (x 10^3 mm^{-3})
JII-268-1	6.76 ± 0.35	8.98 ± 2.77	5.97 ± 1.77
JII-268-2	7.11 ± 0.63	3.83 ± 1.16	2.68 ± 0.79
JII-268-3	9.67 ± 1.14	2.02 ± 1.25	1.69 ± 0.76
JII-268-4	2.47 ± 1.05	2.19 ± 1.40	0.76 ± 0.23
JII-268-5	5.78 ± 0.94	1.93 ± 0.51	1.09 ± 0.16
JII-268-9	--	--	--
JII-268-10	7.93 ± 2.16	1.74 ± 0.81	1.06 ± 0.31
JII-268-11	7.96 ± 0.79	5.01 ± 2.06	3.65 ± 1.28
JII-268-12	8.88 ± 0.78	1.44 ± 0.47	1.25 ± 0.21
JII-268-13	6.27 ± 0.22	13.39 ± 2.56	8.26 ± 1.35
JII-268-14	6.41 ± 0.55	6.82 ± 1.80	4.20 ± 0.92
JII-268-15	10.64 ± 0.43	0.74 ± 0.31	0.78 ± 0.31
JII-268-16	7.03 ± 0.42	2.86 ± 0.59	1.99 ± 0.31
JII-268-17	10.23 ± 0.61	2.09 ± 0.26	2.12 ± 0.19
JII-268-18	8.64 ± 0.42	4.57 ± 0.77	3.87 ± 0.51
JII-268-19	8.32 ± 0.59	3.89 ± 1.36	3.12 ± 0.83
JII-268-20	8.71 ± 0.83	1.56 ± 0.47	1.34 ± 0.33
JII-268-22	10.64 ± 0.66	1.10 ± 0.21	1.17 ± 0.15
JII-268-23	8.04 ± 0.70	4.06 ± 0.81	3.14 ± 0.33
JII-268-24	8.51 ± 0.76	5.18 ± 1.77	4.07 ± 1.19

Table 7. Helium abundances.

	Crushing		Melting				
Sample	$^3He/^4He$	^4He (10^{-6} cm^3 STP/g)	$^3He/^4He$	^4He (10^{-5} cm^3 STP/g)	Total ^4He (10^{-5} cm^3 STP/g)	Fraction ^4He in vesicles	$C/^3He$ (x 10^8)
JII-268-9	8.58 ± 0.12	2.86	8.47 ± 0.13	1.80	2.09	0.14	6.57
JII-268-10	8.58 ± 0.12	1.52	8.51 ± 0.12	1.95	2.10	0.07	6.11
JII-268-11	8.68 ± 0.12	4.27	8.26 ± 0.13	1.64	2.07	0.21	7.02
JII-268-12	8.72 ± 0.13	2.65	8.57 ± 0.13	1.72	1.99	0.13	6.61
JII-268-13	8.41 ± 0.12	7.09	8.33 ± 0.13	1.74	2.44	0.29	6.73
JII-268-14	8.55 ± 0.12	4.33	8.44 ± 0.13	1.70	2.13	0.20	7.11
JII-268-15	8.74 ± 0.13	4.75	8.37 ± 0.13	1.56	2.03	0.23	7.14
JII-268-16	8.68 ± 0.12	3.24	8.45 ± 0.13	1.66	1.98	0.16	7.23
JII-268-17	8.47 ± 0.13	9.75	8.47 ± 0.12	1.03	2.01	0.49	6.94
JII-268-18	8.42 ± 0.13	9.75	8.57 ± 0.12	1.21	2.18	0.45	7.27
JII-268-19	8.39 ± 0.13	8.89	8.56 ± 0.12	1.01	1.89	0.47	7.42
JII-268-20	8.53 ± 0.12	9.95	8.54 ± 0.12	1.10	2.09	0.48	6.58
JII-268-22	8.47 ± 0.12	10.28	8.46 ± 0.12	0.97	2.00	0.52	7.02
JII-268-23	8.45 ± 0.13	9.73	8.42 ± 0.12	1.01	1.98	0.49	6.65
JII-268-24	8.43 ± 0.12	8.19	8.66 ± 0.12	1.23	2.05	0.40	8.48

*He measurements performed with blank levels of 2 – 5 x 10^{-11} cm^3 STP/g.

Table 8. Growth rates determined by constant and decreasing magma velocities.

v_{axis} (m/s)	v_{final} (m/s)	τ (hours)	$G_{maximum}$ (mm/s)	$G_{minimum}$ (mm/s)
0.0001	0.0001	6716	9.91×10^{-9}	3.38×10^{-10}
0.1	0.1	7	9.91×10^{-8}	3.38×10^{-9}
0.0001	0	13433	9.74×10^{-9}	1.72×10^{-10}
0.001	0	1343	9.74×10^{-8}	1.72×10^{-9}
0.01	0	134	9.74×10^{-7}	1.72×10^{-8}
0.1	0	13	9.74×10^{-6}	1.72×10^{-7}